The Pennsylvania State University

The Graduate School

College of Engineering

SEDIMENTS OF SOFT SPHERES ARRANGED BY EFFECTIVE DENSITY

A Thesis in

Chemical Engineering

by

César González Serrano

Submitted in Partial Fulfillment
of the Requirements
for the Degree of

Master of Science

August 2010

The thesis of César González Serrano was reviewed and approved* by the following:

Darrell Velegol
Professor of Chemical Engineering
Thesis Advisor

Kristen Fichthorn
Merrell R. Fenske Professor

Robert Rioux
Friedrich G. Helfferich Assistant Professor

Andrew L. Zydney
Walter L. Robb Chair and Professor of Chemical Engineering
Head of the Department of Department or Graduate Program

*Signatures are on file in the Graduate School

ABSTRACT

Colloidal suspensions often contain mixtures of particles that must be sorted by size or density. One route to sorting gram-size quantities of particles is sedimentation, which has been studied for decades from both dynamic and thermodynamic perspectives. However, an important question remains unanswered: What sediment structure results when bi-disperse or poly-disperse particles settle rapidly, but remain non-glassy in the final dense sediment? This document shows that bi-disperse colloids having soft-sphere interactions spontaneously arrange into two macroscopic layers after a sedimentation process at Peclet number greater than unity. The layering can be explained without appealing to complex hydrodynamic or thermodynamic arguments; rather, the layering is readily explained simply by minimizing the free energy of the system, which is primarily the gravitational energy. The contribution of entropy and interparticle forces to the total energy of the system is negligible. When minimizing the gravitational energy, it has been found that the way that particles pack is a key parameter. However, the particles may start to aggregate under high centrifugal force or great sediment height. This can be a limitation to the particle reordering. The results presented here may lead to designs for preventing de-mixing of colloidal products during shipment, for improving sorting or size-refinement operations for colloidal particles of different size or density, for sorting mixtures of biological components, or for purifying mixtures of colloidal assemblies.

TABLE OF CONTENTS

LIST OF FIGURES

LIST OF TABLES

ACKNOWLEDGEMENTS

Posiblemente no me haya llevado ni dos segundos decidir que esta sección de mi tesis esté escrita en español. ¿Por qué? La razón es simple: ¿de qué me sirve escribir esta sección si los principales destinatarios nunca van a poder leerla? Los primeros a los que debo agradecer son mis padres, sin ellos no podría estar ahora escribiendo estas líneas. Sus valores y educación han forjado la persona que soy y gracias a ello he conseguido grandes logros, por ejemplo esta tesis. Gracias papá, gracias mamá. Junto a mis padres debo agradecer a mis hermanos y demás familia. Todos ellos tienen una parte de mérito en que esto se haya podido producir. Sé que siempre piensan en aquel primo o sobrino que un día decidió "cruzar el charco" o, como dice Isabel, "César, el que se fue en avión muy lejos". Esta tesis está dedicada a vosotros.

Mención especial merece una persona que conocí el primer día que entré en este departamento, y que desde entonces se ha convertido en una parte de mí. Es imposible escribir aquí todo lo que ha hecho por mí en estos dos años. Tu apoyo personal y profesional, tu amor y compañía ha sido un bálsamo en los momentos más duros. Gracias por todo Laura, eres una bendición en mi vida.

También quiero dar gracias al estupendo grupo humano que componen mis compañeros de laboratorio: Neetu Chaturvedi, Huda Jerri, Tso-Yi Chiang, Joseph McDermott y Li-Ju Wang. Además de grandes personas han sido una fuente inagotable de ideas durante todo este proceso. Mención especial requiere Joseph McDermott cuya colaboración en este proyecto ha sido crucial en el desarrollo del mismo. No quiero

olvidarme de la aportación de los estudiantes Matthew Boland, Kristin Ann Wegener y Tawana Hinnes. Su trabajo ha sido una parte muy importante de esta investigación. Me gustaría agradecer al equipo de Penn State's Huck Institute of Life Sciences Center for Qualitative Cell Analysis por el adiestramiento y uso de su Olympus Fluoview 1000 confocal laser scanning microscope.

Agradezco al Department of Energy (Grant No. DE-FG02-07ER46414) la financiación del proyecto. También a SABIC Innovative Platics por darme la oportunidad de hacer este Máster. Siempre han estado a mi lado para ayudarme en todo momento y es algo que aprecio sinceramente.

Por último, a mi tutor el Profesor Darrell Velegol. Él ha sido la mente brillante que ha guiado este proyecto desde el principio. Durante todo este tiempo se ha ganado mi respeto y admiración no sólo como profesional sino también como ser humano. Gracias por ser un perfecto capitán manteniendo el rumbo de este proyecto y llevándolo a buen puerto.

Chapter 1

Introduction

1.1 Motivation

Fabrication of colloidal assemblies and nanostructured materials with functional properties has received considerable attention in the last 50 years. Colloidal particles are interesting building blocks to create ordered and complex materials with applications on chemical engineering, pharmacy, physics and biology.[1] The possibilities with colloidal assemblies are almost endless, from simple doublets created by joining two particles together[2] to colloidal crystals that present spectacular optical properties and are formed by thousands of particles[3].

Velegol's laboratory group expertise lies on producing colloidal assemblies. However, the separation of these colloidal assemblies from unreacted colloidal precursors or side products[2,4,5] is a limitation to scale this technology. In fact, many other research groups around the world face the same issue[6,7,8] (Figure 1.1).

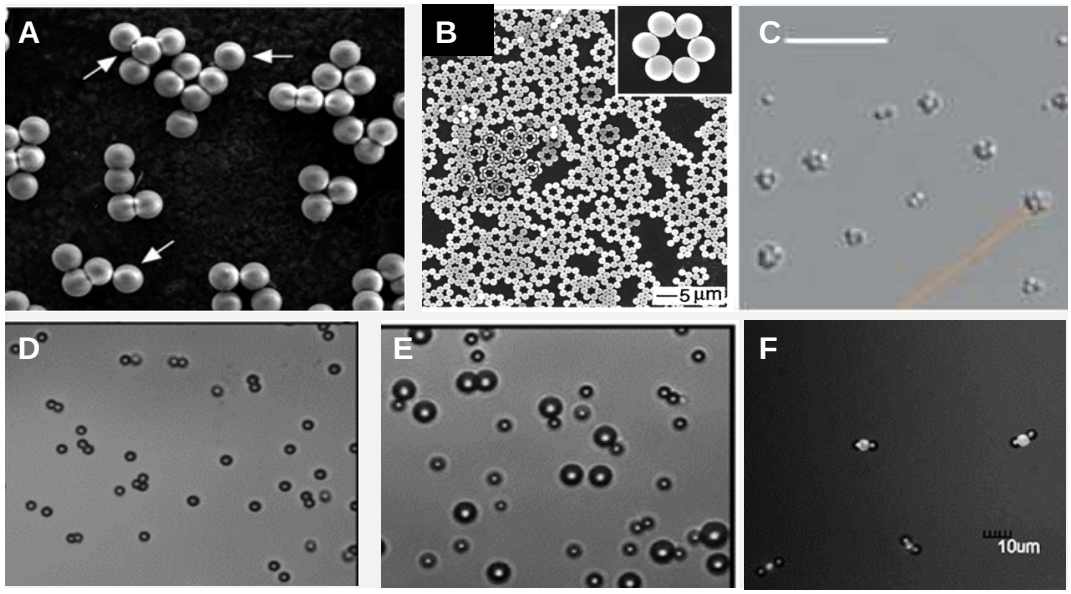

Figure 1.1 Examples of particles that require separation. Assemblies from the groups of **A** van Blaaderen[8], **B** Xia[7], **C** Pine[6], and **D-F** Velegol[5,9]. All have proper assemblies mixed with other particles (none shown in **F**). These require particle sorting.

Separation of colloidal particles in the range of 10 nm to 10 μm by size or shape, which we will call here "sorting", is a challenging process, especially in a commercial scale, constituting a bottleneck for the scale-up of colloidal technology. High throughput techniques are usually designed to separate particles from the suspending fluid, such as filtration. Sorting operations used in large scale, such as the recovery of bitumen from oil sands[10] or the separation of minerals from ore[11], require distinct differences in surface properties like surface potential or hydrophobicity. However, when dealing with particles of the same surface chemistry, the techniques used are field flow fractionation[12], hydrodynamic chromatography[13], and density gradient centrifugation[14]. In field flow fractionation, particles are allowed to diffuse in the presence of an external field and a parabolic flow profile is applied perpendicular to that field to separate the particles.

Hydrodynamic chromatography, sorts colloids due to their different transport properties inside a column. This column is typically packed with spherical particles. Density centrifugation uses a density gradient to fix complex fluid instabilities of settling colloidal suspensions, and thus the particles sort due to their different settling velocities. All of these techniques present a major disadvantage: the separation rate is lab scale, approximately 1mL/h or less.

During Fall 2008, we were exploring the limits of the density centrifugation technique using mixtures of polystyrene latex (PSL) particles with two different sizes. Once we prepared an excess sample of equal volume of 1 μm white and 2 μm blue sulfate PSL (see Chapter 3 for Material and Methods). After storage of the sample for 24 hours in an Eppendorf tube, we surprisingly observed that the particles seemed to have spontaneously sorted (Figure 1.2). This phenomenon seemed to satisfy all the requirements that we were asking for. These requirements were to obtain particle sorting with a high throughput in an overall simple process. For instance, particles separated in two distinguishable layers and ended up in a concentrated suspension by simply having them settle in a vessel. Furthermore, since gravity is the driving force, the process seemed to speed up by using a higher centrifugal force.

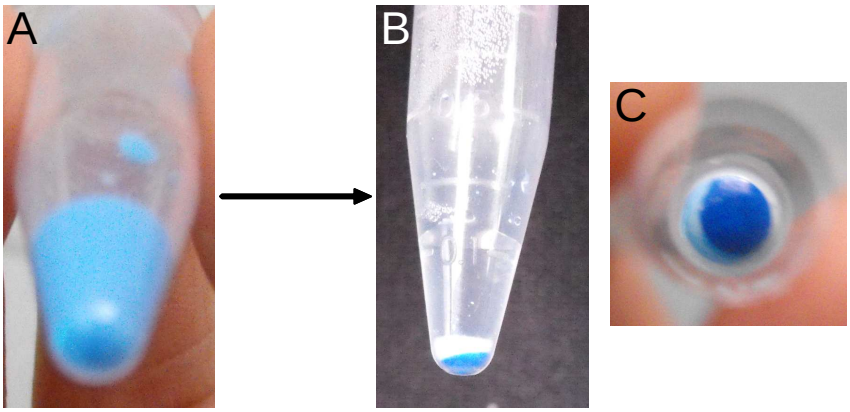

Figure 1.2 Spontaneous sorting of colloidal particles. **A** 200 µL of equal volume mixture of 1 µm white and 2 µm blue sulfate PSL at 0.01 volume fraction. **B** Lateral view of the resulting sediment of **A** after sedimentation at normal gravity (1g) for 24 hours. **C** Bottom view of the same sediment on **B**.

1.2 Objectives

After observing the surprising result shown in Figure 1.2, we decided to examine the physics behind particle sorting thoroughly:

1. Characterize the sediment produced with different mixtures of particles and analyze the composition of the sorted layers.
2. Identify the parameters (e.g., particle density, particle radius, gravitational force…) that are influencing the separation process, characterize the role they are playing in this particle sorting technique, and discover the possible limitations of the process.
3. Elaborate a model that allows us to predict the outcome of different mixtures and find the optimal combination of variables to perform each separation in a fast, easy, and clean way.

1.3 References

[1] Caruso, F. *Adv. Mater*. **13**, 11-22 (2001)

[2] Yake, Allison M.; Panella, Rocco A.; Snyder, Charles E.; Velegol, Darrell. *Langmuir*, **22**, 9135-9141 (2006).

[3] P. N. Pusey, W. Van Megen, *Nature*, **320**, 340-342 (1986).

[4] Snyder, Charles E.; Yake, Allison M.; Feick, Jason D.; Velegol, Darrell. *Langmuir*, **21**, 4813-4815 (2005).

[5] Yake, Allison M.; Snyder, Charles E.; Velegol, Darrell. *Langmuir*, **23**, 9069-9075 (2007).

[6] Manoharan, Vinothan N.; Elsesser, Mark T.; Pine, David J. *Science*, **301**, 483-487 (2003).

[7] Yin, Y.; Lu, Y.; Gates, B.; Xia, Y *J. Am. Chem. Soc*., **123**, 8718-8729 (2001).

[8] Johnson, van Kats, van Blaaderen. *Langmuir* **21**, 11510-11517 (2005).

[9] Snyder, C. E.; Ong, M.; Velegol, D. *Soft Matter* **5**, 1263-1268 (2009).

[10] Tu, Y.; O'Carroll, J.B.; Kotlyar, L.S.; Sparks, B.D.; Ng, S.; Chung, K.H.; Cuddy, G. *Fuel*, **84**, 653-660 (2005).

[11] G.D. Sharma and Mahendra K. Sharma (Eds.), (Springer, New York 1992).

[12] Giddings, J.C.; Yang, F.J.; Myers, M.N. *Science*, **193**, 1244-1245 (1976).

[13] Small, H. *J. Colloid Int. Sci.* **48**, 147-161 (1974)

[14] Manoharan, V.N.; Elsesser, M.T.; Pine, D.J. *Science*, **301**, 483-487 (2003).

Chapter 2

Background

In this chapter we will review the necessary concepts to understand some of the physics behind the sedimentation of the blue and white particles shown in Figure 1.2. First, we will take a look at the studies regarding the settling speed of colloidal suspensions. We will also review how the dynamics of colloidal sedimentation have been used to solve the problem of sorting colloidal assemblies. Since colloidal particles accumulate at the bottom of the vessel and pack, we will review the parameters influencing particle packing. Then we will analyze how colloidal particle follow those trends of particle packing. Finally, we will present initial hypotheses about our colloidal system based on the literature reviewed.

2.1 Sedimentation Rate of Colloidal Particles

Particle sedimentation is a common phenomenon in nature that has been used in many industrial applications such as solid-fluid separations and purification processes. Among these applications are dewatering of coal slurries and clarification of waste water. The broad knowledge on this field has allowed the design of many types of equipment based on this technique such as gravity settlers, thickeners, clarifiers, and centrifuges.

Much research has been done to understand and predict the behavior of colloidal sedimentation. The first approach was derived by Stokes[1] at low *Re* number by balancing the gravitational and drag forces, obtaining the following expression for the isolated sphere velocity U_0.

$$U_0 = \frac{2a^2(\rho_p - \rho)g}{9\eta} \tag{2.1}$$

Where a represents the particle radius, ρ_p and ρ are the particle and fluid densities respectively, η is the fluid viscosity and g is the gravitational acceleration. However, this result only applies to an isolated sphere, which it is not our experimental case. From this starting point, the complexities of concentrated suspensions have been studied from the experimental[2] and phenomenological point of view. Batchelor[3] analyzed the problem considering two body interactions, but his results only apply up to volume fraction ϕ = 0.03. Brady and Durlofsky[4] derived a model considering monodisperse samples with multi-body interactions and applied the results from dilute suspensions up to the close packed limit. Russel et al.[5] considered the particle interaction potential to obtain a semi-empirical model:

$$\frac{U}{U_0} = (1-\phi)^{-K} \tag{2.2}$$

Where the value of K accounts for the hydrodynamic and the collective interactions. As it was pointed by Batchelor[6], Batchelor and Wen[7], and Jansen et al.[8]: K = -0.655 + 0.44α, being α the interaction parameter to account for the interparticle potentials.

Batchelor[6] and Batchelor and Wen[7] analyzed the influence of polydispersity, but no reliable methods currently exist for high concentrated suspensions. Xu et al.[9] showed that depletion forces have a significant influence in the particle settling velocity, especially for a large particle size ratio. In the case of charged spheres, the influence of the electrostatic field caused by the charge separation generated by the different settling velocities of the particles and the ions has been also addressed.[10,11] More detailed reviews of the state of art of colloidal sedimentation can be found in the manuscripts by Davis and Acrivos[12] and Vesaratchanon et al.[13].

This broad knowledge on colloidal sedimentation has also been applied for particle-particle separations. This is the case of the Density Gradient Centrifugation.

2.2 Density Gradient Centrifugation

In 1951 Brakke[14] published an article about Density Gradient Centrifugation as a new technique that could be used to separate colloidal particles based on their settling velocities. The objective of the density gradient is allowing the particles to settle as individual entities instead of having a suspension behaving as a complex fluid[5]. The method consists on building a density gradient on a column of fluid. This can be achieved for example by placing a concentrated suspension of sucrose at the bottom of the vessel and just pure DI water on top, the sucrose will start to diffuse upwards creating a concentration gradient that results also in a density gradient. Then the particle solution can be added on top of the column. Next, centrifuge the system to increase the settling velocities. If the particles settle at different speeds, due to either size and/or density, they will travel different distances on the column producing distinct bands (Figure 2.1). More

information about how to apply this technique can be found in the books by Price[15] and Hinton and Dobrota[16].

This technique has also been successfully applied to sorting of colloidal assemblies by Manoharan et al.[17] obtaining a high purity separation (Figure 2.1).

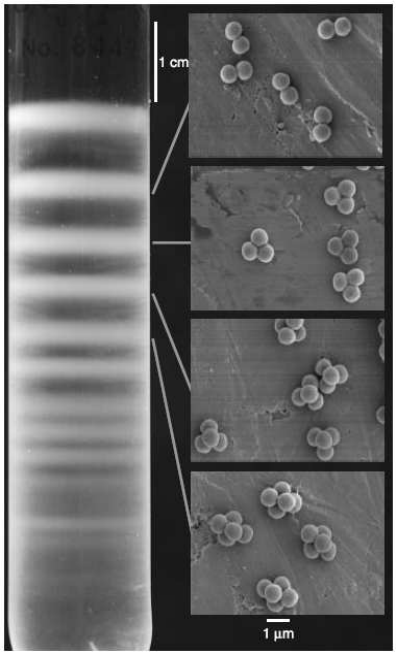

Figure 2.1 Density gradient centrifugation of a mixture with different colloidal assemblies. Notice that each band corresponds to a different type of assembly. The band appears according to the size of the colloidal assembly that each contains.[17]

However, the application of density gradient centrifugation has a major challenge. When loading particle suspensions with a volume fraction higher than 10^{-3} or 10^{-4}, convective instability occurs and the particles end up mixed throughout the sedimentation vessel (Figure 2.2A,B,C). During the sedimentation dynamics of colloidal particles, circulation patterns have been observed[18] (Figure 2.2 D). These convective cells are

qualitatively quite similar to the convection rolls seen in the classic Rayleigh-Bénard instability[19] (Figure 2.2 E).

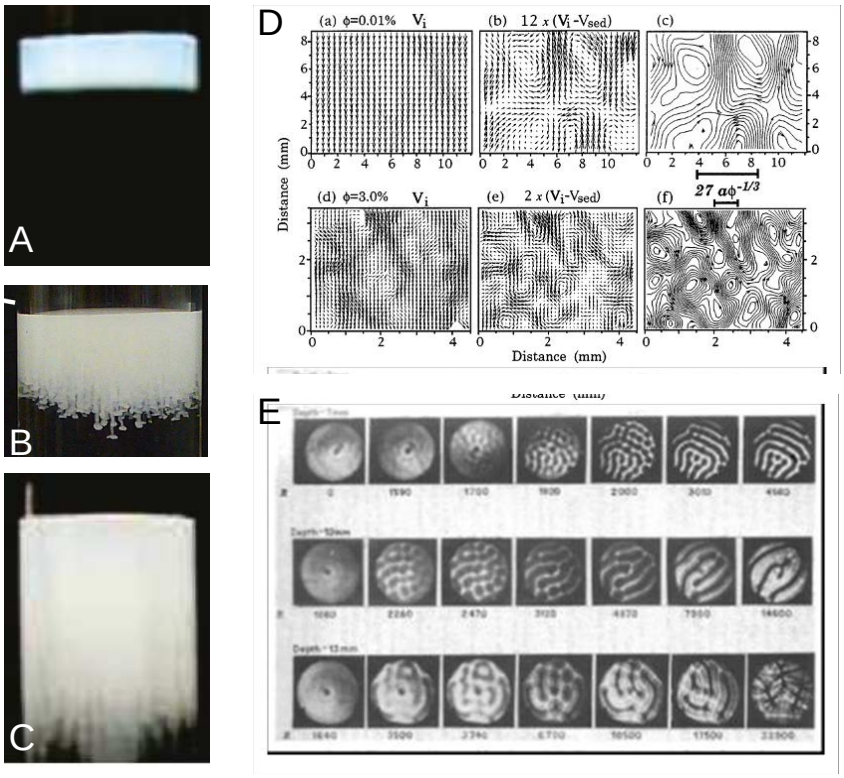

Figure 2.2 Instabilities in density gradient centrifugation. **A** 0.01 volume fraction suspension of particles on top of a sucrose density gradient at time $t = 0$. **B** At time t = 15 min, tendril-like structures have formed. **C** At time t = 1 h, the tube holds a well-mixed suspension.[20]. **D** Velocimetry images showing swirls extending over millimeter-scale distances in colloidal sedimentation.[18] **E** Circulation patterns observed in classic Rayleigh-Bénard instability.[19]

Jerri et al.[20] applied the theory of the Rayleigh-Bénard instability to sedimentation. They found that no instability is developed until a critical Rayleigh number R_c is exceeded.

$$R = \frac{-g\frac{\partial \rho}{\partial z}h^4}{D_s \eta_S} < R_c \qquad (2.3)$$

Where R is the Rayleigh number for sedimentation, z is the coordinate along the settling direction, h is the depth of the density inversion, D_s in the diffusivity of the sucrose, and η_s the viscosity of the local sucrose solution. $R_c = 658$ was found as the limit to stability.

The limit imposed to the usable volume fraction for density gradient centrifugation is a problem for scaling up the technology. Furthermore, these limitations also apply to any sorting method that uses a force monopole on the particles, including magnetophoresis, dielectrophoresis, and possibly electrophoresis.[20]

Our case, as we saw in Figure 1.2, is different from Density Gradient Centrifugation. In our system, all the particles reach the bottom of the recipient. They start to accumulate and pack. But how efficiently do particles pack?

2.3 Particle Packing

Particle packing is also an ancient topic with implications in many disciplines such as jamming of granular materials[21], glasses[22], and crystal-glass phase transitions[23]. In determining the packing fraction of a certain sample, it is important to know how many particle-particle contacts are required to mechanically stabilize the sample[24], which for a sphere is ≈ 6. There are two critical parameters that play an essential role here: polydispersity and shape. As a consequence, packing fraction values lie within a wide range. For example, the random packing of monodisperse spheres[25] is 0.64, in the case of

bidisperse spheres[26] it can be as high as 0.825, and octahedra[27] can even pack up to 0.947. Table 2.1 provides a summary of the packing fraction values for different particle types.

Table 2.1 Packing fraction values for different particle types.

Configuration	Type of particle	Packing fraction	Reference
Random loose packing	Monodisperse spheres	0.555	Onoda & Liniger *Phys. Rev. Lett.* 1990[28]
Random packing	Monodisperse spheres	0.64	Berryman J. G. *Physical Review A* 1983.[25]
	Binary mixture of spheres. Maximum value	0.825	Visscher & Bolsterli *Nature* 1972.[26]
	Prolate Ellipsoids Aspect ratio = 2	0.715	Donev et al. *Science* 2004.[24]
	Oblate Ellipsoids Aspect ratio = 0.5	0.684	Donev et al. *Science* 2004.[24]
	M&M candies	0.71	Donev et al. *Science* 2004.[24]
	Penny coins	0.574	Chaikin et al. *Ind Eng Chem Res.* 2006.[29]
	Tetrahedra	0.6817	Shui-Xiang et al. *Chin. Phys. Lett.* 2008[30]
	Octahedra	0.947	Torquato & Jiao. *Nature* 2009.[27]
	Superballs		Jiao et al. *Phys. Rev. E* 2009.[31]
	Cut spheres		Wouterse et al. *J. Phys.: Condens. Matter* 2007.[32]
FCC	Monodisperse spheres	$\pi/\sqrt{18}$ = 0.7405	Hales *Ann. Math.* 2005.[33]
BCC	Monodisperse spheres	0.68	Sanders & Gibson_Material Science and Engineering_2003[34]

Computer simulations[24, 32] have shown the influence of the particle shape in the packing fraction by varying the aspect ratio of spheroid particles as it can be seen from Figure 2.3.

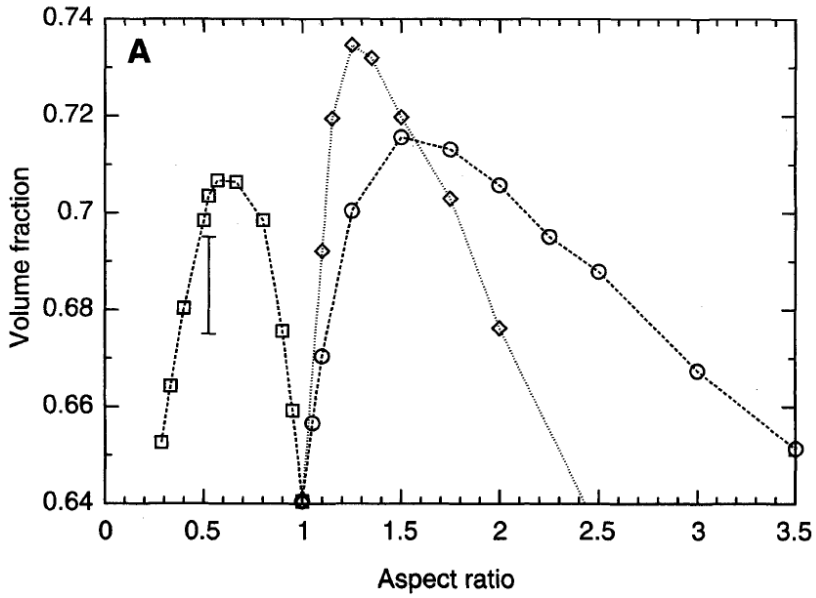

Figure 2.3 Influence of the aspect ratio on the packing fraction of prolate (circles), oblate (squares) and a fully apherical (diamonds) spheroids.[24]

The polydispersity and the proportions of each particle size also affect the value of the packing fraction. Studies on bidisperse mixtures of spheres have been carried out since 1960 both experimentally[35] and with computer simulations[26]. An interesting result from these studies is the fact that the highest packing fraction in a bidisperse sample of spheres always corresponds to a mixture (Figure 2.4). Some studies have also shown different ways to study the packing fraction of samples with different polydispersities.[36, 37, 38]

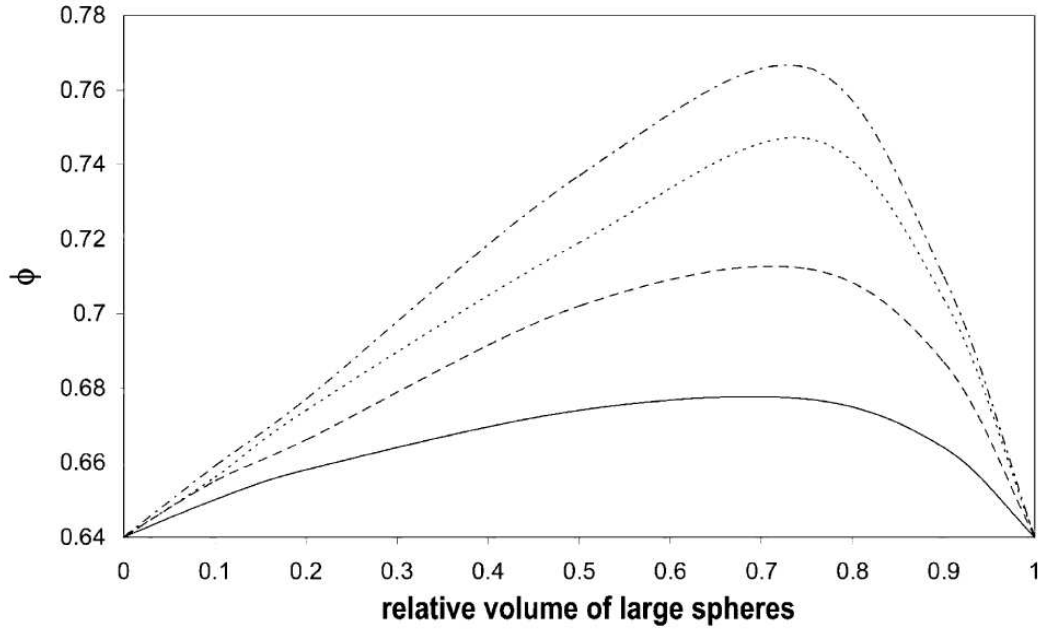

Figure 2.4 Packing fraction versus relative volume fraction of large spheres in bidisperse packings with radius ratios 2 (——), 3 (− − −), 4 (· · ·), 5 (− · −).[39]

The packing fraction of mixtures of singlets and doublets were studied by Kristin Ann Wegener and Tawana Hines during Summer 2009 with the guidance of Darrell Velegol, Joseph J. McDermott, and myself, César González Serrano. The results of the work have been included in Appendix 3 and a discussion is included in Chapter 6.

Some of the concepts related to particle packing have also been applied to colloidal science. In the next section we will discuss the peculiarities of colloidal packing.

2.4 Colloidal Packing

In the case of colloidal particles, the way that the particles accumulate and pack is a relatively new field of study. Let us start with the simplest case: monodisperse hard spheres. When the concentration of a suspension of hard spheres starts to increase, the volume fraction of solids goes under different phase transitions. When the volume fraction overcomes 0.494, some of the particles start to produce crystal structures that coexist with free particles in solution. At volume fractions between 0.545 and 0.7404 the most favorable phase is the FCC crystal[40] (Figure 2.5) However, if the volume fraction is increased rapidly and the system does not have time to form the crystal, a glass is obtained.

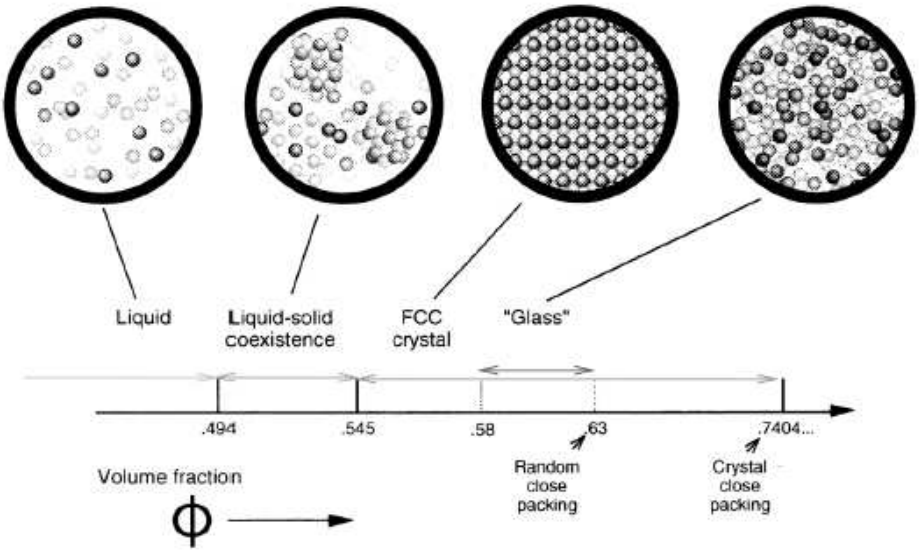

Figure 2.5 Equilibrium phase diagram from computer simulation for uniformly sized hard spheres.[41]

In the case of repulsive spheres a surprising result arises. Since the particles interact through electrostatic forces, they can feel each other at higher separations. Thus, the disorder-order transition takes place at a much lower volume fraction (Figure 2.6).[42]

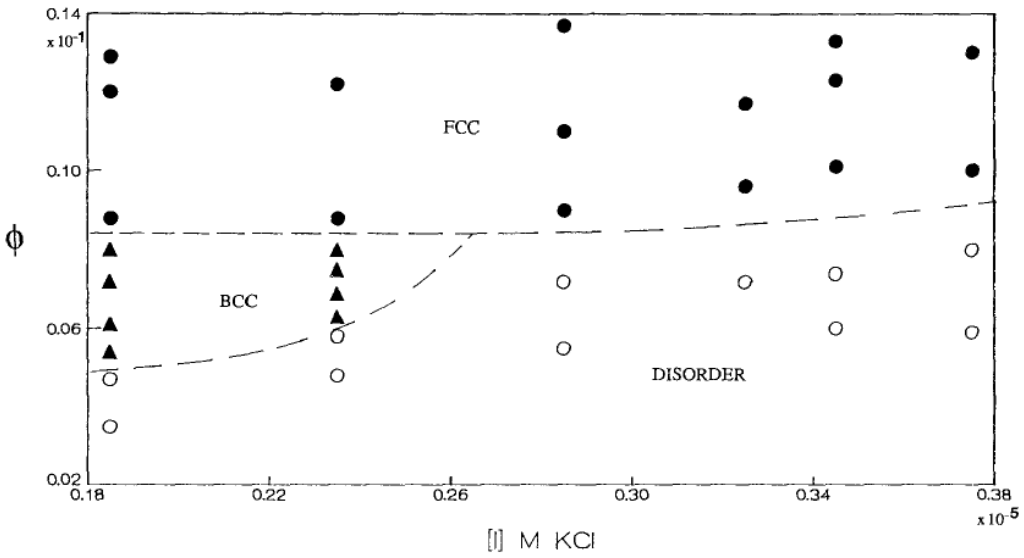

Figure 2.6 Experimental phase diagram at low ionic strength for 66.7 nm radius PSL particles with ζ-potential 64±3.9 mV (value independent of volume fraction in the range of the graph).[42]

Phase diagrams also exist for the case of bidisperse suspensions, even in the case of charged particles.[43] In these systems the structure of the crystal depends both on the size and number ratio between large and small particles.[44] Since colloidal particles are an excellent model to study atomic packing and phase transitions, all of these studies of colloidal packing are performed in conditions such that gravity has no effect. However, Zhu et al. reported that gravity has a significant influence in the crystal formation.[45]

In our case, the colloidal packing is produced by concentrating the suspension using sedimentation. Under these conditions there is a key parameter to determine the sediment nature, the *Pe* number[46]. The *Pe* number is defined as:

$$Pe = \frac{a^3(\rho - \rho_p)g}{kT} \tag{2.4}$$

Where k is Boltzmann's constant and T is the temperature. *Pe* represents the competition between the rate of particle sedimentation and particle diffusion. If $Pe \ll 1$, then a crystal is obtained. However, if $Pe \gg 1$, then the resulting sediment will be glassy. Other parameter that plays an important role on the sediment formation is the initial volume fraction of the settling suspension.[47]

The influence of the polydispersity on the sediment nature has recently been addressed. Martin et al.[48] and Royall et al.[49] studied bidisperse samples of hard spheres and they found that particle polydispersity clearly delays or prevents the crystal formation.

2.5 Hypotheses

After studying the literature on colloidal sedimentation and particle packing, we can formulate hypotheses about what is happening in Figure 1.2. These hypotheses will be tested experimentally in the following chapters of this thesis.

- The large particles settle faster than the small ones. It will be more likely to find a higher concentration of the large particles at the bottom of the sediment than at the top. A complete prediction of the sediment using settling dynamics is challenging due to the multiple body interactions of dissimilar spheres.

- Since the particles are charged, the electrostatic repulsion will prevent interparticle contact. The sediment will be mobile. Furthermore, the particles are settling at $Pe > 1$. Therefore, the sediment will probably be glassy.
- We have a bidisperse mixture of colloidal particles. If the particles packed efficiently to maximize the volume occupied by particles, we may find a mixture of both particle types in the sediment.

2.6 References

[1] Stokes, GG. *Trans Camb. Philos. So.*, **8,** 287 (1845).

[2] Richardson, J.F., Zaki, W.N. *Trans. Inst. Chem. Eng.* **32**, 35-53 (1954).

[3] Batchelor, G.K. *J. Fluid. Mech.* **52** 145 (1972).

[4] Brady, J.F., Durlofsky, L. *J. Phys. Fluids* **31**, 717 (1988).

[5] Russel, W.B., Schowalter, W.R. & Saville, D.A. *Colloidal Dispersions* (Cambridge Univ. Press, Cambridge, 1999).

[6] Batchelor, G.K. *J. Fluid. Mech.* **119**, 379 (1982).

[7] Batchelor, G.K, Wen, C.S. *J. Fluid. Mech.* **124**, 495 (1982).

[8] Jansen, J.W., de Kriuf, C.G., Vrij, A. *J. Colloid Interface Sci.* **114**, 501 (1986).

[9] Xu,W., Nikolov, A.D., Wasan, D.T. *AIChE* **43**, 3215 (1997).

[10] Rasa, M., Philipse, A. P. *Nature* **429**, 857-860 (2004).

[11] Wang, T., Li, H., Sheng, Y., Tsao, H *J. Chem. Phys.* **129**, 204504 (2008).

[12] Davis, R. H., Acrivos, A., *Ann. Rev. Fluid Mech.* **17**, 91-118 (1985)

[13] Vesaratchanon, S., Nikolov, A., Wasan, D. T. *Adv. Colloid Interfac.* **134**, 268-278 (2007).

[14] Brakke, M.K. *J. Am. Chem. Soc.* **73**, 1847-1848 (1951).

[15] Price, C.A. *Centrifugation in Density Gradients*, Academic Press (New York) 1982.

[16] Hinton, R.; Dobrota, M. *Density Gradient Centrifugation*, Elsevier (North-Holland) 1976.

[17] Manoharan, V.N., Elsesser, M.T., Pine, D.J. *Science* **301**, 483-487 (2003).

[18] Segrè, P.N., Herbolzheimer, E., Chaikin, P.M. *Phys. Rev. Lett.* **79**, 2574-2577 (1997).

[19] Lord Rayleigh *Philos. Mag.* **32**, 529-546 (1916).

[20] Jerri, H.A., Sheehan, W.P., Snyder, C.E., Velegol, D. *Langmuir* **26**, 4725-4731 (2010).

[21] Liu, A.J., Nagel, S.R. *Nature* **396**, 21 (1998).

[22] Zallen, R. *The Physics of Amorphous Solids* (Wliey, New York, 1983).

[23] Chaikin, P.M. *Soft and Fragile Matter, Nonequilibrium Dynamics, Metastability and Flow*, M.E. Cates, M.R. Evans, Eds. (Institute of Physics, London, 2000).

[24] Donev, A., Cisse, I., Sachs, D., Variano, E.V., Stillinger, F.H., Connelly, R., Torquato, S., Chaikin, P.M. *Science* **303**, 990-993 (2004).

[25] Berryman, J.G., *Phys. Rev. A* **27**, 1053-1061 (1983).

[26] Visscher, W.M., Bolsterli, M. *Nature* **239**, 504 (1972).

[27] Torquato, S., Jiao, Y. *Nature* **460**, 876-879 (2009).

[28] Onoda, G.Y., Liniger, E.G. *Phys. Rev. Lett.* **64**, 2727-2730 (1990).

[29] Chaikin, P.M., Donev, A., Man, W., Stillinger, F.H., Torquato, S. *Ind. Eng. Chem. Res.* **45**, 6960-6965 (2006).

[30] Shui-Xiang, L., Jian, Z., Xuan, Z. *Chin. Phys. Lett.* **25**, 1724-1726 (2008).

[31] Jiao, Y., Stillinger, F.H., Torquato, S. *Phys. Rev. E.* **79**, 041309 (2009).

[32] Wouterse A., Williams, S.R., Philipse, A.P., *J. Phys.: Condens. Matter* **19**, 406215 (2007).

[33] Hales, T.C., *Ann. Math.* **162**, 1065 (2005).

[34] Sanders, W.S., Gibson, L.J. *Mater. Sci. Eng., A* **352**, 150-161 (2003).

[35] Yerazunis, S.W., Cornell, S.W., Wintner, B. *Nature* **207**, 835-837 (1965).

[36] Schertl, W., Sillescu, H. *J. Stat. Phys.* **77**, 1007-1025 (1994).

[37] Kansal, A.R., Torquato, S., Stillinger, F.H. *J. Chem. Phys.* **117**, 8212-8218 (2002).

[38] Clusel, M., Corwin, E.I., Siemens, A.O.N., Brujić, J. *Nature* **460**, 611-616 (2009).

[39] Lochmann, K., Oger, L., Stoyan, D. *Solid State Sci.* **8**, 1397-1413 (2006).

[40] Mau, S.C., Huse, D.A. *Phys. Rev. E* **59**, 4396-4401 (1999).

[41] Cheng, Z., Chaikin, P.M., Russel, W.B., Meyer, W.V., Zgu, J., Rogers, R.B., Ottewill, R.H. *Mater. Des.* **22**, 529-534 (2001).

[42] Monovoukas, Y., Gast, A.P., *J. Colloid Interface Sci.* **128**, 533-548 (1989).

[43] Meller, A., Stavans, *J. Phys. Rev. Lett.* **68**, 3646-3649 (1992).

[44] Eldridge, M.D., Madden, P.A., Pusey, P.N., Barlett, P. *Mol. Phys.* **84**, 395 (1995).

[45] Zhu, J., Li, M., Rogers, R., Meyer, W., Ottewill, R.H., STS-73 Space Shuttle Crew, Russel, W.B., Chaikin, P.M. *Nature* **387**, 883-885 (1997).

[46] Kim, H., Rajagopalan, R. *J. Mater. Sci. Lett.* **20**, 1545-1547 (2001).

[47] Hoogenboom, J.P., Derks, D., Vergeer, P., van Blaaderen, A. *J. Chem. Phys.* **117**, 11320-11328 (2002).

[48] Martin, S., Bryant, G., van Megen, W. *Phys. Rev. E* **71**, 021404 (2205).

[49] Royall, C.P., Vermolen, E.CM., van Blaaderen, A., Tanaka, H. *J. Phys.: Condens. Matter* **20**, 404225 (2008).

Chapter 3

Materials and Methods

3.1 Materials

The polymer particles used to study colloidal packing were monodisperse, surfactant-free, sulfate-functionalized polystyrene latex (S-PSL) microspheres with different sizes. Monodisperse silica particles and gold nanoparticles were also used for the experiments. These gold particles (150 nm average diameter) were produced by Joseph J. McDermott from the reduction in solutions of gold ions with gum arabic over 1 hour as described by Handley[1]. A full description of the particles used and their characteristics can be found in Table 3.1.

Table 3.1 Particle specifications and characteristics.

Diameter (μm)	CV	Material	Color	ζ-potential in DI water (mV)	Company	Batch #
0.99	2.5%	S-PSL	White	-58.36 ± 5.23	Interfacial Dynamics Corporation (IDC)	8890,1
2.0	2.60%	S-PSL	Green	-43.81 ± 3.11	IDC	1-GN-2K.
2.0	2.50%	S-PSL	Blue	-49.72 ± 4.32	IDC	
2.0	1.30%	S-PSL	Fluorescent-Yellow-Green	-51.71 ± 3.11	IDC	21515W
3.0	3.50%	S-PSL	Red	-57.46 ± 4.15	IDC	1-RE-3K.1
3.0	3.70%	S-PSL	Green	-63.06 ± 3.65	IDC	
4.0	5.1%	S-PSL	White	-55.83 ± 5.11	IDC	1932,1
4.0	2.30%	S-PSL	Fluorescent-Red	-81.40 ± 1.21	IDC	646220
4.9	4.40%	S-PSL	White	-61.92 ± 5.76	IDC	2434R,1
0.9	N/A	Silica	White	-65.45 ± 4.53	Bangs Laboratories	4949
3.01	N/A	Silica	White	-62.37 ± 6.57	Bangs Laboratories	5411
0.15	N/A	Gold	Brown		N/A	

The Pyrex Pasteur Pipettes were obtained from VWR International (West Chester, PA). The centrifuge tubes used were BLUE MAX™ Jr. 15mL Polypropylene Conical Tubes bought from BD Falcon™ (Franklin Lakes, NJ). The DI water that was used for all experiments and washing steps (Millipore Corp. Milli-Q system) had a specific resistance greater than 1 MΩ•cm (i.e., "equilibrium water", due to dissolved CO_2).

3.2 Instrumentation

The optical microscopy images were obtained on a Nikon Eclipse TE2000-U inverted optical microscope. The Confocal and different interference contrast (DIC) images were captured on an Olympus Fluoview 1000 Confocal Laser Scanning Confocal Microscope with a 60× oil objective at the Huck Institute of the Life Sciences Center for Quantitative Cell Analysis. The ultrasonicator is from VWR International (model 550T). The zeta potential measurements were taken using a Zeta Potential Phase Analysis Light Scattering instrument (ZetaPALS) from Brookhaven Instruments Corporation. For the centrifugation process, a Sorvall® Biofuge Primo Centrifuge was used. The VM-3000 mini vortexer was bought from VWR International.

3.3 ζ-potential measurements

The instrument must be turned on 1 hour before taking measurements in order to allow the system to equilibrate the temperature at 25.0 ± 1.3 ºC. The particles samples were prepared by diluting 10 µL of original bottle suspension in 10 ml of DI water. The electrode of the instrument was cleaned with ethanol and rinsed with DI water. The cuvette was introduced in the instrument where the measurements were performed by using five runs with twenty-five cycles per run.

3.4 Sample mixtures preparation

Particle suspensions of 1 mL at 0.01 volume fraction were prepared for the following particles: 0.99 µm sulfate PSL, 2.0 µm sulfate PSL, 3.0 µm sulfate PSL, 4.0 µm sulfate PSL, 4.9 µm sulfate PSL, 3.0 µm silica and 0.9 µm silica. The particles suspensions were prepared in an Eppendorf tube by diluting the original concentration of the bottle to 0.01 volume fraction adding DI water. Then 200 mL of 2 µm sulfate PSL were poured together with 200 mL of 3 µm sulfate PSL into another Eppendorf tube, mixed using a vortexer for 5 minutes and placed in the ultrasonicator for 15 minutes to break any possible aggregates. The same procedure was used for all the binary mixtures mentioned in this document.

3.5 Sedimentation experiments

The mixture was transferred into a Pasteur pipette whose bottom had been previously sealed with wax. A Pasteur pipette was used instead of a capillary tube because it provides a narrow capillary in order to study the sediment and a large reservoir

at the top to load a larger amount of suspension. The Pasteur pipette was mounted into a centrifuge tube in order to keep it straight along its vertical axis. Then the centrifuge tube can be kept settling at normal gravity or it can be introduced into the centrifuge in order to increase the centrifugal force up to 1000 times the normal gravity (1000g). In order to recover the sediment and analyze it, the Pasteur pipette was removed from the centrifuge tube and the sediment was extracted with a needle. The sediment layers were resuspended in DI water and placed in the ultrasonicator for 15 minutes to break any aggregates. Then, the particles were analyzed with an optical microscope using a 40× air objective. A diagram of the overall sorting technique is displayed in Figure 3.1.

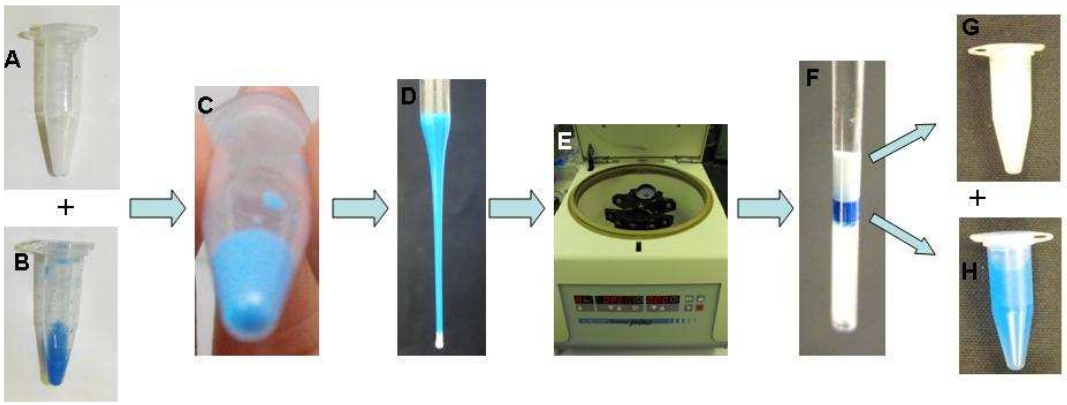

Figure 3.1 Effective density sorting technique. **A** Suspension of 0.01 volume fraction of 0.99 μm sulfate PSL particles. **B** Suspension of 0.01 volume fraction of 2.0 μm particles. **C** Homogeneous mixture of the suspensions in **A** and **B**. **D** Suspension in **C** introduced into a glass Pasteur Pipette whose bottom has been previously sealed with wax (see the white region at the bottom of the pipette). **E** Centrifuge used for the sedimentation experiments (the pipette in **D** can also be kept straight at normal gravity instead of using the centrifuge). **F** Resulting sediment after centrifugation of the sample in **D**. **G** Recovered top white region of the sediment in **F**. **H** Recovered bottom blue region of the sediment in **F.**

3.6 Confocal microscope sample preparation

A mixture of 60 µL with equal volumes of 4.0 µm red fluorescent sulfate PSL and 2.0 µm yellow-green fluorescent sulfate PSL particles at 2% solids is placed in a rectangular capillary tube 0.20×2.0×50 mm RT3520 bought from VitroCom (Mt. Lakes, NJ). The capillary tube is sealed with optical resin and allowed to rest on the 2.0 mm side slightly tilted with respect to the gravity vector (see Figure 3.2). The particles were allowed to settle for 2 weeks. Confocal images of sediment were taken with a 60× oil objective at different positions of the capillary.

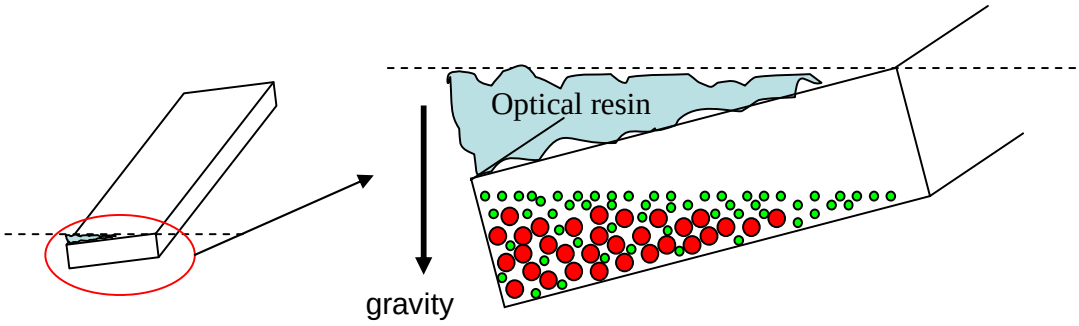

Figure 3.2 Schematic representation of the capillary prepared for confocal microscopy. Notice that the presence of optical resin (in the figure, blue residue on top of the capillary) tilts the capillary tube with respect to the gravity vector.

3.7 References

[1] Handley, D.A. “Colloidal Gold: Principles, Methods and Applications”, M. A. Hayat, Ed. (Academic Press, San Diego, 1989), vol. 1.

Chapter 4

Experimental Analysis of Sediments of Bidisperse Interacting Spheres

In this chapter we will analyze experimentally the sediment composition. Furthermore, we will explore the influence of different variables on the sediment composition. Among these variables we will consider:

- Particle size ratio
- Particle density
- Initial volume fraction
- Gravity

Finally, we will also see some evidences of the particle movement in the packed configuration and we will draw some direct conclusions from these experiments.

4.1 Characterize the sediment composition

In order to analyze and study the settling behavior of charged colloidal particles, we developed the technique described in Section 3.5. By using this technique it is possible to identify the different regions of the sediment and recover them for further analysis with optical microscopy. We first analyzed the sample of Figure 1.2: 0.01 volume fraction of equal volume of 2 μm blue sulfate PSL and 1 μm white sulfate PSL settling at 1g (Figure 4.1).

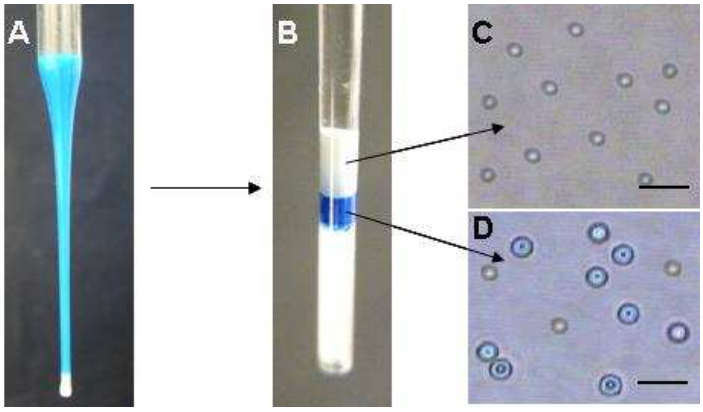

Figure 4.1 Analysis of the sediment composition produced by sedimentation at 1g of a mixture of 2 μm and 1 μm sulfate PSL. All the scale bars at the bottom right of the images C and D are 5 μm. **A** Mixture with equal volume of 2 μm blue and 1 μm white sulfate PSL particles at an initial volume fraction $\phi = 0.01$. **B** Resulting sediment of **A** after sedimentation at normal gravity (1g) for 7 days. The white region at the bottom is wax sealing the glass capillary. **C** Optical microscopy image of the white region of the sediment in **B** after dilution with DI water. All the particles are 1 μm white PSL. **D** Optical microscopy image of the blue region of the sediment in **B** after dilution with DI water. The image shows a mixture of 2 μm and 1 μm sulfate PSL particles.

The particle recovery of the experiment displayed in Figure 4.1 provided us with information about the sediment composition. The top layer of the sediment was composed exclusively of 1 μm white particles as it can be seen from Figure 4.1C. On the other hand, the bottom layer of the sediment was composed of a mixture from both particles (Figure 4.1D). Although this result could be explained just by Stokes velocity (eq. 2.1), we will carefully analyze the influence of different variables on the sediment composition before extracting any conclusions.

We need to point out that the actual recovery method described in Section 3.5 does not allow a perfect recovery of the layers. Extracting the particles using a syringe creates some mixture between the layers, making the composition analysis challenging. The top layer can be easily recovered without creating much retromixing. However, the recovery of the bottom layer is more demanding. Images of the recoveries from the experiments in this section are included in Appendix A.

4.2 Particle size ratio

If we want to apply the fundamentals of this discovery to sort particles with different sizes it is important to check how the particle size ratio affects the resulting sediment. In order to make this analysis, several experiments for different particle size ratio, at constant particle density, were run (Table 4.1).

Table 4.1 Experiments run to analyze the influence of the particle size ratio on the sediment composition.

Run#	Material	Size (μm)	g Force	Relative Volume	Volume Fraction
1	Sulfate PSL - Sulfate PSL	1 – 2	1	1:1	0.01
2	Sulfate PSL - Sulfate PSL	2 – 3	1	1:1	0.01
3	Sulfate PSL - Sulfate PSL	2 – 4	1	1:1	0.01
4	Sulfate PSL - Sulfate PSL	2 - 4.9	1	1:1	0.01
5	Sulfate PSL - Sulfate PSL	3 – 4	1	1:1	0.01
6	Sulfate PSL - Sulfate PSL	3 – 4.9	1	1:1	0.01

All the results from these experiments showed that the basic structure of the sediment does not change with the particle size ratio (see Figure 4.2). The top region of the sediment always consisted of a pure phase of small particles. However, the lower region of the sediment always consists of a mixture from both types of particles, with a

higher concentration of the large ones. The actual proportions of each particle depend on the particles used during the settling process (see Appendix A for data).

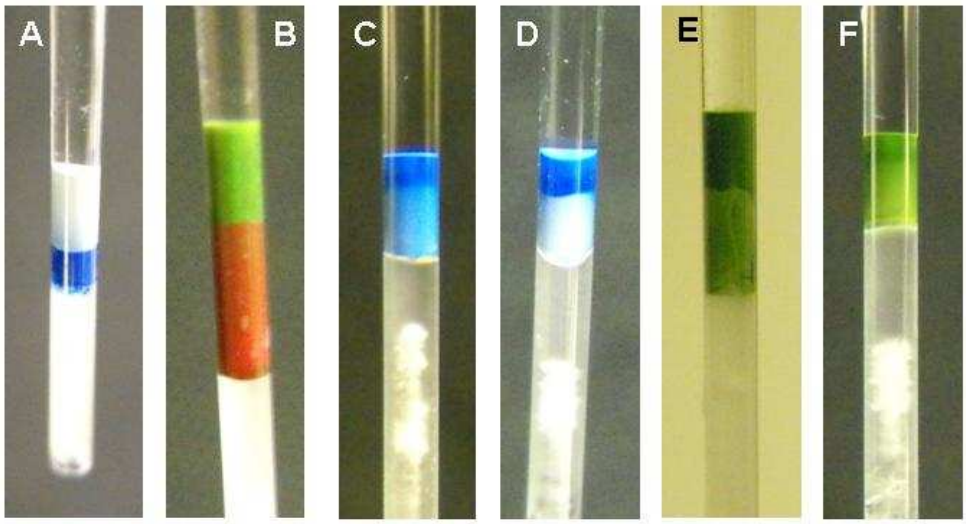

Figure 4.2 Sediments of sulfate PSL binary mixtures with different particle size ratio. **A** 2 μm blue and 1 μm white sulfate PSL. **B** 3 μm red and 2 μm green sulfate PSL. **C** 4 μm white and 2 μm blue sulfate PSL. **D** 4.9 μm white and 2 μm blue sulfate PSL. **E** 4 μm white and 3 μm green sulfate PSL. **F** 4.9 μm white and 3 μm green sulfate PSL.

4.3 Particle density

In all the cases presented up to this point, the particles used were made of the same material. However, it would be interesting to evaluate the behavior of sediments composed of particles with different densities. Silica, PSL and gold particles have been used for this purpose (Table 4.2). These materials have been selected in order to explore different density ratios but always keeping a negative surface potential on the particles. The particles used should not have opposite charges to avoid particle aggregation in the bulk fluid.

Table 4.2 Experiments run to analyze the influence of the particle density on the sediment composition.

Run#	Material	Size (μm)	g Force	Relative Volume	Volume Fraction
7	Sulfate PSL – Silica	3 – 3	1	1:1	0.01
8	Sulfate PSL – Silica	3 – 3	1000	1:1	0.01
9	Sulfate PSL – Silica	3 – 3	1	9:1	0.01
10	Sulfate PSL – Silica	4 – 3	1	1:1	0.01
11	Sulfate PSL – Gold	4.9 – 0.150	1000		0.01
12	Sulfate PSL – Gold	4.9 – 0.150	1		0.01

In all cases the densest phase is always found at the bottom of the sediment (Figure 4.3). In the case of the silica and PSL (Fig 4.3A,B,C&D) the bottom layer is always composed of pure silica and the top layer is always composed of pure PSL. This perfect separation is always found regardless of the centrifugal force applied and the relative proportion of particles in the mixture.

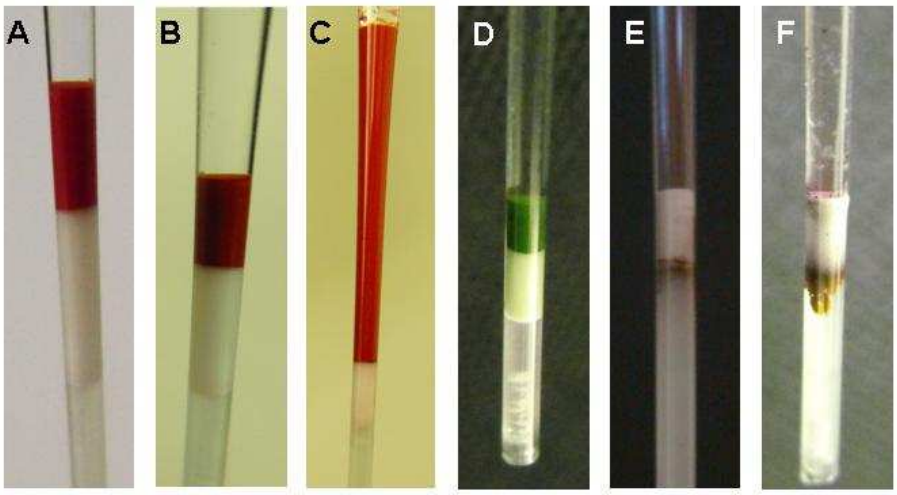

Figure 4.3 Sediments of binary mixtures of colloidal particles with different particle densities. **A** Equal volume of 3 μm red sulfate PSL and 3 μm white silica settled at 1g. **B** Equal volume of 3 μm red sulfate PSL and 3 μm white silica settled at 1000g. **C** 9:1 volume ratio of 3 μm red sulfate PSL and 3 μm white silica settled at 1g. **D** Equal volume of 3 μm green sulfate PSL and 0.9 μm white silica settled at 1g. **E** Equal volume of 4.9 μm white sulfate PSL and 150 nm gold settled at 1000g. **F** Equal volume of 4.9 μm white sulfate PSL and 150 nm gold settled at 1g.

Special attention is required for the cases of 4 μm sulfate PSL and 150 nm gold (Figure 4.3E&F). The gold particles have a higher density than silica, but they settle slower due to their small size. However, at the end of both experiments the gold nanoparticles were found at the bottom of the sediment.

4.4 Initial volume fraction

The influence of the initial volume fraction of particles in the crystal formation by particle settling has been reported in the literature (see Section 2.3). In this section, we want to analyze if the initial volume fraction of particles has any influence on the

sediment produced. Up to this point we have always used 0.01 volume fraction because we are interested in concentrated suspensions. However, in this section we will experiment with different volume fractions. The experiments run to study this variable are displayed in Table 4.3.

Table 4.3 Experiments run to analyze the influence of the initial volume fraction of particles on the sediment composition.

Run#	Material	Size (μm)	g Force	Relative Volume	Volume Fraction
13	Sulfate PSL - Sulfate PSL	2 – 4	1	1:1	0.001
14	Sulfate PSL - Sulfate PSL	2 – 4	1	1:1	0.0001
15	Sulfate PSL - Sulfate PSL	2 – 3	1	1:1	0.0001
17	Sulfate PSL - Silica	3 – 3	1	1:1	0.0001

Although the recovery was impossible to perform for a volume fraction of 10^{-4}, the sediment composition seems to qualitatively be similar in all cases (Figure 4.4). No significant difference has been observed for different particle size ratios and different particle density ratios.

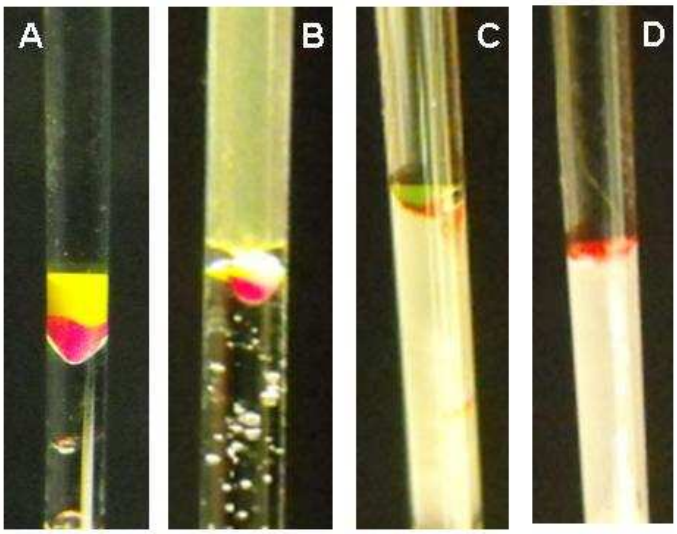

Figure 4.4 Sediments of binary mixtures of colloidal particles with different initial volume fractions. **A** 4 μm fluorescent red sulfate PSL and 2 μm fluorescent yellow-green sulfate PSL at initial volume fraction $\phi = 0.001$. **B** 4 μm fluorescent red sulfate PSL and 2 μm fluorescent yellow-green sulfate PSL at initial volume fraction $\phi = 0.0001$. **C** 3 μm red and 2 μm green sulfate PSL at initial volume fraction $\phi = 0.0001$. **D** 3 μm red sulfate PSL and 3 μm white silica at initial volume fraction $\phi = 0.0001$.

4.5 Gravity

The gravitational/centrifugal force is a key parameter to speed up the separation process. According to Stokes settling velocity (eq. 2.1) the sedimentation rate is directly proportional to the gravitational/centrifugal force. If the experiment can be performed at a high centrifugal acceleration, the separation time can be reduced from days or hours to minutes. However, it is important to check how such increase in the gravitational force is going to affect the sediment composition. In order to analyze the influence of gravity in the sediment composition the experiments shown in Table 4.4 were performed.

Table 4.4 Experiments run to analyze the influence of the gravitational/centrifugal force on the sediment formation.

Run#	Material	Size (μm)	g Force	Relative Volume	Volume Fraction
18	Sulfate PSL - Sulfate PSL	2 – 3	1	1:1	0.01
19	Sulfate PSL - Sulfate PSL	2 – 3	10	1:1	0.01
20	Sulfate PSL - Sulfate PSL	2 – 3	100	1:1	0.01
21	Sulfate PSL - Sulfate PSL	2 – 3	1000	1:1	0.01

An important result was observed at high values of the gravitational force. When the experiment was run with the particles settling at 1g or 10g, the resulting sediment was mobile. Under these conditions the particles still flowed, they could be extracted with a syringe and the particles move if the pipette is tilted. However, when the experiment was run with the particles setting at 1000g or 100g they accumulate at the bottom producing a solid pellet. Under these conditions the sediment produced was totally rigid, except for a few particles at the top. The particles in the sediment did not flow and they could not be recovered with a syringe, but by breaking the capillary. The observation of the solid pellet under optical microscopy revealed that the particles were aggregated (see Figure 4.5).

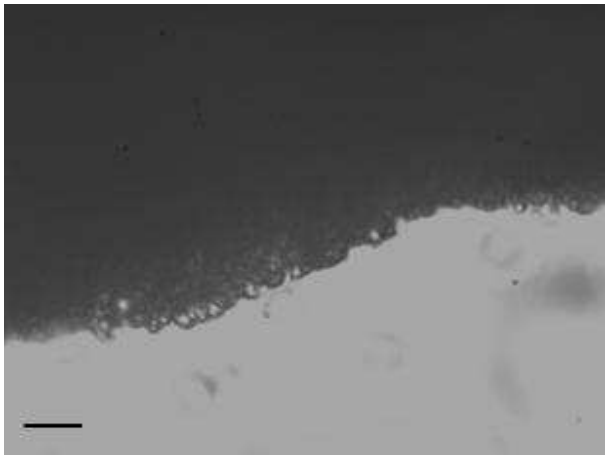

Figure 4.5 Optical microscopy image of the sediment produced by a mixture of 2 and 3 μm sulfate PSL settling at 1000g. During the recovery process the sediment was always kept in solution. No sonication was performed in this recovery. The scale bar is 10 μm.

The influence of gravity on the aggregation of colloids has been reported previously in the literature.[1,2] It takes place when the electrostatic repulsion between particles is overcame by the gravitational force. A deeper analysis of the physics behind this phenomenon will be done in Chapter 5. What these experiments prove is that the aggregation at a high centrifugal force has a remarkable importance in the sediment configuration. As a consequence, this effect has to be taken into account if we want to apply this technique for separation purposes.

4.6 Evidence of particle mobility

Studying the particle behavior is key in understanding the mechanisms that influence the sediment formation. At this point all the experiments that we tried basically consisted of a homogenously distributed bidisperse mixture settling to produce a sediment. In order to study the particle behavior, a different type of experiment was

performed. Now, we are going to settle the small particles first and produce a sediment, then we will settle the big particles on top of that sediment. What will be the final configuration of this sediment? We discovered that it depends on multiple conditions. Table 4.5 shows the experiments that were run to study particle behavior.

Table 4.5 Experiments run to analyze the influence of the particle mobility sediment composition.

Run#	Particle 1	g Force	Particle 2	g Force
22	2 μm Sulfate PSL	1	3 μm Sulfate PSL	1
23	2 μm Sulfate PSL	1000	3 μm Sulfate PSL	1000
24	2 μm Sulfate PSL	1000	3 μm Sulfate PSL	1

Each of these cases needs to be analyzed individually. First, let us consider Run # 22, where we sediment both types of particles at 1g (Figure 4.6).

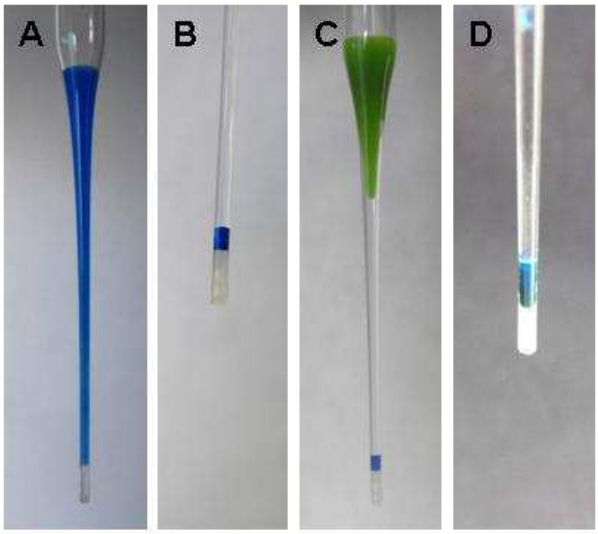

Figure 4.6 Particle reorganization during the sediment formation. **A** 100 mL of 2 μm blue sulfate PSL particles at 0.01 volume fraction were loaded into a glass Pasteur pipette sealed with wax. **B** sediment produced after the suspension in **A** settled for 3 days at 1g. **C** 100 mL of 3 μm green sulfate PSL particles at 0.01 volume fraction were loaded on top of the sediment in **B**. **D** Final configuration of the system after the 3 μm green particles were settled at 1g for 5 days on top of the sediment produced on **B**. At the end, the 2 μm blue particles rose to the top.

As it can be seen from Figure 4.6, there is particle movement, a reorganization in the sediment. Taking a closer look at the image shown in Figure 4.6D, it is possible to notice that the top of the sediment was composed by blue 2 μm particles – the ones that we settled first. On the other hand, it can be seen how the green particles have gone through the initial blue sediment producing a mixture. This result is critical for the subsequent discussion in Section 4.8. It provides a solid evidence of particle movement and reorganization during the sediment formation. Let us analyze Run # 23, where we sediment both types of particles at 1000g (Figure 4.7).

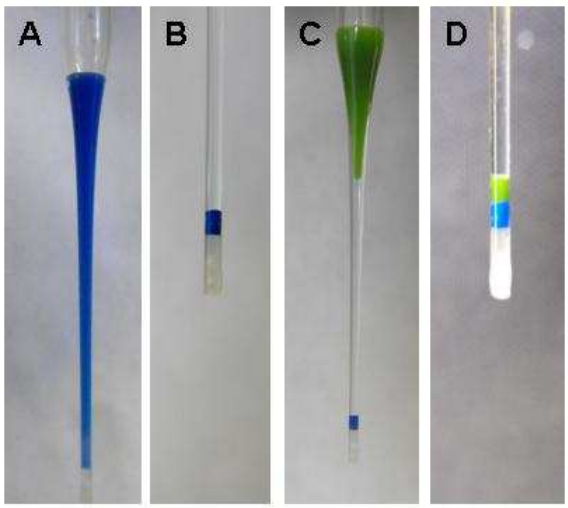

Figure 4.7 Particle freezing at high g values. **A** 100 mL of 2 μm blue sulfate PSL particles at 0.01 volume fraction were loaded into a glass Pasteur pipette sealed with wax. **B** Sediment produced after centrifugation of the suspension in **A** at 1000g for 30 minutes. **C** 100 mL of 3 μm green sulfate PSL particles at 0.01 volume fraction were loaded on top of the sediment in **B**. **D** Final configuration of the system after the 3 μm green particles were centrifuged at 1000g for 30 minutes on top of the sediment produced in **C**. This system remained unchanged for over 12 months.

As it can be seen from Figure 4.7D, settling both particles at 1000g leads to a completely different result. In this case, there is no particle reorganization. The blue particles were settled first and they remained at the bottom. On the other hand, the green particles were settled on top and they did not go through the blue ones. This result can be explained by considering the influence of gravity on the particle aggregation (see Section 4.5). In the first sediment produced with the blue particles, the gravitational force pulls the particles together and thereby causing aggregation. Since the blue particles are aggregated, when the green particles reach the sediment, they cannot penetrate and they

just produce another aggregated sediment on top of the blue one. Finally, let us take a look at Run # 24. What will happen if we first settle the blue particles at 1000g and then the green ones on top at 1g (Figure 4.8)?

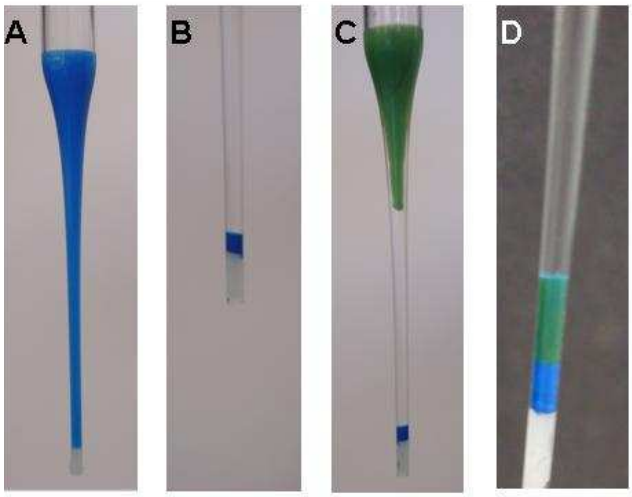

Figure 4.8 Particle freezing and reordering at mixed g values. **A** 100 mL of 2 μm blue sulfate PSL particles at 0.01 volume fraction were loaded into a glass Pasteur pipette sealed with wax. **B** Sediment produced after centrifugation of the suspension in **A** at 1000g for 30 minutes. **C** 100 mL of 3 μm green sulfate PSL particles at 0.01 volume fraction were loaded on top of the sediment in **B**. **D** Final configuration of the system after the 3 μm green particles were settled at 1g for 5 days on top of the sediment produced in **B**.

The result from Figure 4.8 requires a deeper analysis, although it is based on principles from the previous experiments (aggregation at high g values and particle reorganization at low g values). When the blue particles settle at 1000g they produced a sediment where most of the particles are aggregated. However, the top layers did not aggregate because they do not have many particles on the top squeezing them. When the

green particles are settled at 1g, the top layers of the blue particles can still move. As a consequence, the blue particles that are not aggregated reorganize with the green ones and some of them merge to the top.

4.7 Diffusion of soft spheres in the packed state

We strongly believe that the charged nature of our colloidal system is playing an important role in the particle reorganization seen in the previous section. It has been shown that for packed hard-sphere colloidal sediments, particle diffusion coefficients are effectively zero.[3] However, for interacting, repulsive spheres, diffusion coefficients increase at lower ionic strength, even at high volume fractions.[4] Non-zero diffusion coefficients perhaps allow for our sediments to rearrange themselves.

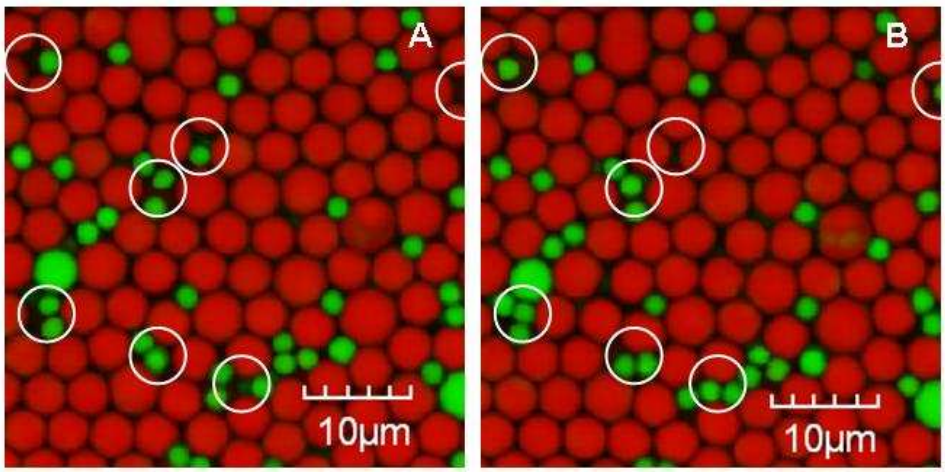

Figure 4.9 Particle diffusion. Confocal fluorescent microscopy images overlay of a sediment produced with 4 μm red fluorescent PSL and 2 μm yellow-green fluorescent PSL. The images **A** and **B** were taken at the same point in the sediment 5 seconds apart. Notice that there is a significant amount of particle movement, especially of the small green particles, which move in and out of the focal plane. The particles with the highest mobility have been highlighted to guide the reader.

Actually we can estimate the soft sphere diffusion coefficient in this system with the evidence of particle mobility shown in Figure 4.9. Fick's second law of diffusion provides us the distance traveled for a particle by diffusion in a given period of time Δt.

$$\frac{\partial n}{\partial t} = D\nabla^2 n$$
$$\left\langle \Delta x^2 + \Delta y^2 \right\rangle = 4D\Delta t \qquad (4.1)$$

Where n represents the concentration of particles, D is the diffusion coefficient, and $\langle \Delta x^2 + \Delta y^2 \rangle$ is the average root-mean-square (rms) distance traveled. This result is given for the distance traveled in 2 dimensions. In the case of the 2 μm yellow-green fluorescent PSL particles, the estimate of the diffusion coefficient gives a value of $(3.56 \pm 0.43) \times 10^{-15}$ m^2/s. In the case of the 4 μm red fluorescent PSL the particle movement is much lower and a good estimate cannot be obtained with the resolution of confocal microscopy.

4.8 Discussion about the leading mechanism

After the experimental characterization of the sediment composition and the studies of the particle mobility we can draw some conclusions about the particle behavior. First, we are going to test the hypothesis that we formulated in Section 2.5:

- *It will be more likely to find a higher concentration of the large particles at the bottom of the sediment than at the top.* As it was proved in Section 4.1, the bottom layer of the sediment consisted of a mixture of both type of particles with a higher

volume fraction of the large ones. On the other hand, the top layer of the sediment consisted of pure small particles.

- *The sediment will be mobile and probably glassy.* As we saw in Section 4.6, if the particles settle at low g values, i.e. 1g, the sediment is mobile and particle reorganization was observed. On the other hand, if the gravitational force overcomes the interparticle repulsion, the particles will aggregate in the sediment. Neither of the experiments in this chapter has produced iridescent sediments, even after 6 months of resting. The iridescent phenomenon is characteristic of the crystal structures.[5] As a consequence, we can conclude that the sediments obtained were randomly packed structures.
- *We may find a mixture of both particle types in the sediment.* In Section 4.1, we saw that the bottom layer of the sediment actually consisted of a mixture of both types of particles. However, the discussion about packing efficiency will be done in Chapter 5.

As it can be seen most of the hypotheses formulated from the existing literature revealed to be correct. Now, we are going to extract some implications from the experimental results found in this chapter.

Initially we hypothesized that the configuration of the blue and white particles (Figure 1.2) could be explained by the infinite-dilution sedimentation rate, visualizing that whenever any particle reached the interface, it remained frozen in place. If this was true, then the number ratio of particles in the lower sediment region should be $x_1/x_2 = \left(u_1 n_1^0\right) / \left(u_2 n_2^0\right)$, where u_1 and u_2 are the Stokes settling speeds of particles 1 and

2 respectively, and n_1^0 and n_2^0 are the initial number fractions. However, this prediction contradicts the result seen in the PSL-silica experiments (Section 4.4). During the sedimentation of mixtures with silica and PSL particles, the resulting sediment always consisted of two pure phases. Importantly, the same exclusive arrangement was found even with an initial mixture of 90% PSL and 10% silica by volume. In this case the value of x_{silica}/x_{PSL} is equal to 2.35, which it is not clearly the experimental case.

It is clear that the sediment composition cannot be predicted just with Stokes settling velocity. However, as we explained in Section 2.1, the settling behavior of our concentrated charged colloidal system is way too complex to be only explained by the Stokes equation. One may argue that the backflow produced during the particle sedimentation is creating the perfect separation for silica and PSL. Even that would be hard to verify due to the complexities of the multibody interactions between particles. However, there is one result that cannot be explained just by using colloidal settling dynamics. This is the result from the experiment shown in Figure 4.7. That particle reorganization suggests that the sediment is evolving to a certain state. Indeed, the precise sorting seen in this silica-PSL experiment appears to be a thermodynamic separation result. All of the densest particles are at the bottom, while all of the least dense ones are on top.

Furthermore, the sharp line demarcating the two regions indicates a non-Boltzmann distribution of the particles. According to Boltzmann, the probability density that one particle is at height z is $p(z) \propto \exp(-mgz/kT)$. Therefore, the average height of the particles in a container of height L can be calculated as:

$$\bar{z} = \frac{\int_0^L z e^{-mgz/kT} dz}{\int_0^L e^{-mgz/kT} dz} = \frac{kT}{mg}\left(1 - \frac{L}{e^{mgL/kT} - 1}\right) \qquad (4.2)$$

Where m is the mass of a colloidal particle. In the case of a system of PSL colloidal particles of 1 μm radius settling in water at normal gravity at 293 K, the expression of the average height can be simplified as:

$$\bar{z} = \frac{kT}{mg} \qquad (4.3)$$

In the system previously mentioned the value of the average height is $\bar{z}$ = 1.74 μm. If the particle composition within the sediment was given by Boltzmann, then an exponential decay of the particle composition with gravity would be expected. However, as the value $\bar{z}$ indicates, the exponential decay is in the order of microns, while the sediment itself is in the order of mm or even cm. As a consequence, the particle concentration in the sediment cannot be an exponential decay over a height of mm or cm. Furthermore, the Boltzmann distribution applies to non-interacting particles, which is clearly not the case of the charged colloidal particles that we are using. The result we observe experimentally is decidedly a non-Boltzmann distribution.

Our hypothesis is that the sediment composition is dictated by the minimum potential energy state. This theory and its modeling are discussed in Chapter 5.

4.9 References

[1] Meijer, A.E.J., van Megen, W.J., Lyklema, J. *J. Colloid Interface Sci.* **66**, 99-104 (1978).

[2] Bensley, C. N., Hunter, R. J. *J. Colloid Interface Sci.* **92**, 448-462 (1983).

[3] Kegel, W. K., van Blaaderen, A. *Science* **287,** 290-293 (2000).

[4] Anderson, J. L., Rauh, F., Morales, K. *J. Phys. Chem.* **82**, 608-616 (1978).

[5] Rastogi, V., Melle, S., Calderón, O.G., García, A.A., Marquez M., Velev, O.D. *Adv. Mater.* **20**, 4263-4268 (2008).

Chapter 5

Theory of the Effective Density and the Minimum Potential Energy

As we presented in Section 4.8 the sediment composition does not follow a rate-based prediction or a Boltzmann distribution. The main goal of this chapter is develop a model that is able to explain the experimental results of Chapter 4 and that can be used to predict the outcome of new experiments. Our hypothesis is that the sediment composition can be predicted by **minimizing the free energy of the system, which is primarily the gravitational potential energy**, as we will demonstrate in this chapter. In order to get to the analysis of the potential energy of the system, we will study its following properties:

- The soft sphere nature of charged particles
- Effective density packing of soft spheres
- Model of the minimum free energy:
    - Gravitational potential energy
    - Entropy of mixing
    - Interparticle forces
    - The limitation: particle aggregation due to gravity

5.1 The soft sphere nature of charged particles

Maybe the first question that we should ask ourselves is: why are the colloidal particles charged? Colloidal particles, as almost any surface immersed in water or any

other ionic fluid, become charged. This occurs either by surface group dissociation, metal ion substitution, or adsorption of ions from solution.[1] In the case of the sulfate PSL particles in water, the charge comes from the hydrogen dissociation on the sulfate group[1]. The charge from silica particles in water comes from the dissociation of the silanol groups[2]. For gold particles, the charge comes from the ions chloride or citrate used in their production[3]. As the ζ-potential measurements revealed, our particles are strongly charged, with surface potentials greater than $\left|50\right|$ mV. In order to neutralize the fixed charges formed on the surface of the particles, the ions in the solvent diffuse to the proximity of the particles forming the electrical double layer (see Fig 5.1). The thickness of this electrical double layer is usually represented by the Debye length κ^{-1}. In the case of a Z:Z electrolyte the Debye length is calculated as:

$$\kappa^2 \equiv \frac{2n_\infty Z^2 e^2}{\varepsilon kT} \tag{5.1}$$

Where n_∞ is the ion pairs concentration in the bulk fluid, Z is the valence of the ions, e represents the proton charge, and ε is the dielectric permittivity of the medium. In a packed system, when the particle concentration is high, the effect of the density of counter ions and the reduction in the fluid volume due to the presence of particles modify the actual value of the Debye length.[4]

$$\kappa^2 = \frac{e^2}{\varepsilon kT}\frac{2Z^2 n_\infty - \frac{3qZ\phi}{ae}}{1-\phi} \tag{5.2}$$

$$q = 2\left(2\varepsilon kTn_\infty\right)^{1/2}\sinh\left(\frac{eZ\psi_s}{2kT}\right) \tag{5.3}$$

Where ϕ is the volume fraction occupied by the particles in the suspension, q is the surface charge density and ψ_s is the electrical potential in the surface of the particle.

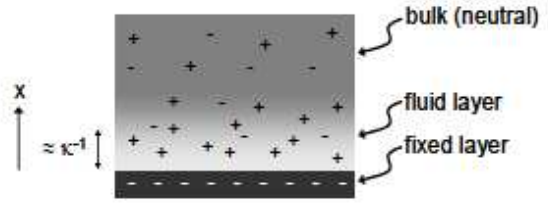

Figure 5.1 Electrical double layer (EDL). The "fixed charge layer" has charges bound to the surface, while the "fluid charge layer" has counter-ions, and a few co-ions, nearby solution.[5]

The charge on the particle will create electrostatic repulsion between the particles. If we neglect the effect of gravity, we will consider it in Section 5.3.6, this electrostatic repulsion is high enough to prevent particle aggregation. As a consequence, the particles cannot come close enough to touch each other. In other words, they do not behave as hard spheres. The point of closest approach of the particles *d* can be derived from the Gibbs free energy and the electrostatic interaction in a concentrated system.[4] In any case, that distance can be expressed as a certain number c_1 times the Debye length κ^{-1}:

$$d = c_1 \times \kappa^{-1} \tag{5.4}$$

5.2 Effective density packing of soft spheres

If we consider that the closest approach between two particles is given by twice the distance *d*, then we can define a soft-sphere radius as:

$$a_{soft} = a + d = a + c_1 \times \kappa^{-1} \tag{5.5}$$

A schematic diagram of how two soft spheres can approach each other is given in Figure 5.2.

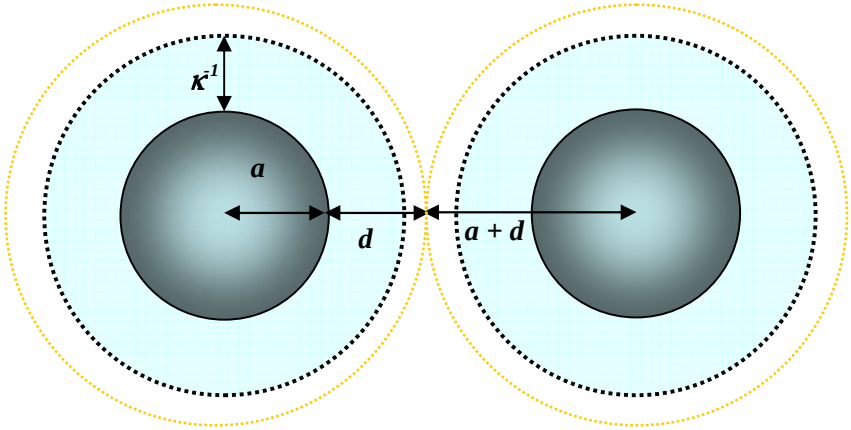

Figure 5.2 Schematic of two soft spheres approaching each other. Notice that in this case both spheres are considered identical.

If we want to calculate the effective density of one of these soft spheres, it is not simply the mass of the particle divided by its volume. Rather, the mass of the soft sphere is given by the mass of the particle plus the mass of fluid within a distance *d* to the surface of the sphere. Similarly the volume of the soft sphere is given by the volume of the particle plus the volume of the fluid shell at a distance *d*. Here, we approximate the effective buoyant density of a single soft sphere as:

$$\rho_{eff} \approx \left(\frac{a}{a + c_1 \times \kappa^{-1}} \right)^3 \left[\rho_p - \rho \right] + \rho \qquad (5.6)$$

In our case we want to know the density value of a sediment formed by a packing of spheres. When multiple sizes of particles pack, the single-particle effective density is not the only important consideration. The density of the sediment also depends on the

packing fraction of the mixture of particles ϕ. In the case of a bidisperse mixture, considering additive volumes, the density of the packing $\rho_{packing}$ can be approximated by:

$$\rho_{packing} \approx \phi\, y \rho_{effL} + \phi(1-y)\rho_{effS} + (1-\phi)\rho \qquad (5.7)$$

Where ρ_{effL} and ρ_{effS} represent the effective density of the soft spheres produced by the large and small particles respectively, and y is the ratio of the volume occupied by the large particles divided by the total volume occupied by all particles. A schematic of the packing produced by soft spheres can be seen in Figure 5.3.

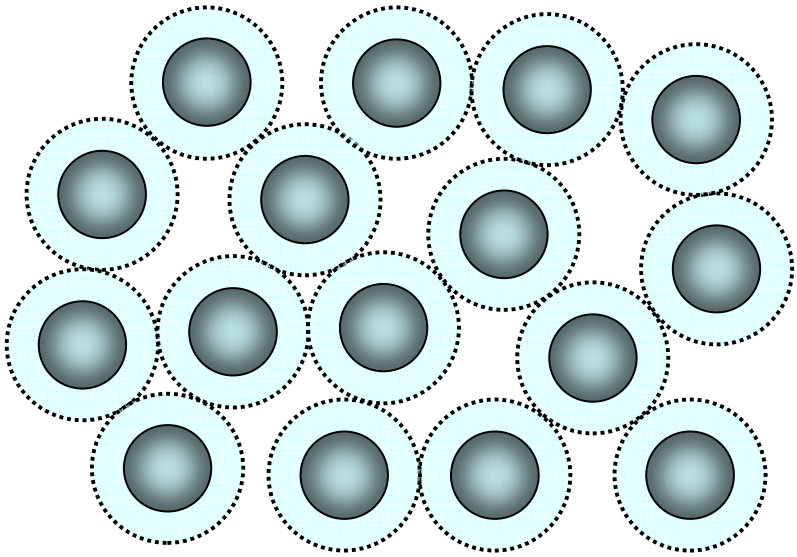

Figure 5.3 Schematic of soft sphere packing. Notice that the closest approach is given by the Debye length, $c_1 = 1$.

The simple result obtained from the packing density calculation, allows us to make quick predictions about sediment composition. Let us calculate the packing density of sediments of PSL and silica particles with different particle size ratios using equation 5.7 and the bidisperse packing fraction values of reference 6 (see Figure 5.4 and Appendix B for data fit).

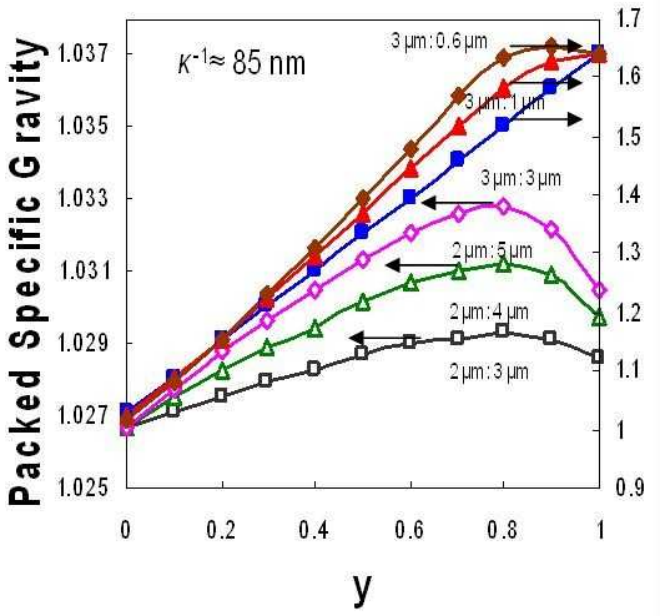

Figure 5.4 Effective specific gravity (SG_{eff}) of binary mixtures of spheres in DI water (from eqs. 5.2, 5.3, 5.6, 5.7 and reference 6). Here, *y* represents the ratio of the volume occupied by the large (or dense) particles divided by the total volume of all particles. The calculation is performed for $d = \kappa^{-1}$. Left axis: SG_{eff} for PSL mixtures: 2 μm – 3 μm (—□—), 2 μm - 4μm (—Δ—) and 2 μm – 5 μm (—◊—). Right axis: SG_{eff} for silica-PSL mixtures: 3 μm Silica – 3 μm PSL (—■—), 3 μm Silica – 1μm PSL (—▲—) and 3 μm Silica – 0.6 μm PSL (—♦—).

There are important results that can be extracted from this graph:

- For mixtures of PSL-PSL particles, the highest possible effective density always consists of a mixture of mostly large particles with some small mixed in. Furthermore, most maxima are near $y = 0.8$. The lowest density phase consists of pure small particles.
- For mixtures of silica-PSL particles, there are two possible outcomes. If the size ratio is close to 1, then the highest possible effective density consists of pure silica

particles. If the size of the PSL particles is much smaller than the size of the silica particles, then the highest possible effective density consists of a mixture of mostly silica particles. The lowest density phase consists of pure PSL particles.

At the beginning of this chapter we mentioned that the sediment composition can be predicted by minimizing the potential energy of the system, but what does that mean? A gross way to see it is thinking about a mixture of water and oil in a decanter. In the case of oil-water, the mixture will separate into two phases: the bottom phase will be mostly water – the densest material and the top phase will be mostly oil – the least dense material. If we consider a sediment of two particle types, it divides into two phases as well: the bottom phase would correspond to the highest possible effective density and the top would be the lowest possible effective density.

We found the following results experimentally. For a PSL-PSL mixture, the densest phase corresponds to a mixture and the least dense phase corresponds to pure small particles. In the case of a silica-PSL mixture, the densest phase corresponds to pure silica and the least dense phase corresponds to pure PSL. Nonetheless, it is important to note that in the oil-water case the phases are not pure due to solubility. Similarly, there is some intermixing between layers in the sediment of particles possibly due to entropy.

This is only a simplified result to make quick predictions about our system. In the next section, we will evaluate the thermodynamics more carefully in order to have a better understanding of the process.

5.3 Model of the minimum free energy

5.3.1 Objectives

In the following section we are going to present a simple model to study sediments of bidisperse soft spheres. The objectives of this model are:

- Calculate the composition on each phase of the sediment
- Calculate the amount of material in each phase
- Identify the limitations of the sedimentation technique

This model has been developed together by Professor Darrell Velegol, Joseph J. McDermott and myself, César González Serrano.

5.3.2 Description of the system

The system that we are considering is a vessel containing a known concentration of bidisperse soft spheres in a fluid media. All the properties of the particles and the fluid are also known. Gravity is acting on the particles, trying to pull them to the bottom of the vessel, and the sediment composition is given by the minimum free energy of the system.

5.3.3 Assumptions

- The whole system is closed, rigid and diathermal (in constant thermal equilibrium with the ambient). In the experimental setup, the Pasteur pipette is rigid, closed, and in thermal equilibrium with the ambient temperature. We can also consider no heat generation or absorption due to interparticle interactions, particle settling, nor

particle mixing. Therefore, there will not be any heat exchange with the ambient temperature.

- The process takes place at a constant temperature and pressure.
- We have two different types of particles in the system. Each of the particle type is monodisperse, both in density and in size. In the experimental setup, the coefficient of variation of each particle type is lower than 5.1% (see Table 3.1).
- Both particles and the fluid media are incompressible. Also, we consider additive volumes in any mixing process. In the experimental setup, we deal with solid PSL, silica, and gold particles in DI water. We are neglecting any dissolution process of the particles in the water. This is a good approximation in the time scale of the experiments.
- The particles have soft sphere interactions. There is always a layer of fluid surrounding them. The soft sphere radius is given by the particle radius plus one time the Debye length, $a+\kappa^{-1}$. In the experimental setup, we are dealing with particles that have a high surface potential. The exact value of interparticle distance will be different in each case due to gravity (see Section 5.3.5), how many particles are interacting, and which particles are interacting. An accurate representation of the system would require considering each particle as an individual entity. We intend to create a simplified model and such complexities are beyond the limits of the model.
- The particles pack into a random close-packed system. It is random because in the experimental setup we never saw crystal structures, as evidenced by a lack of iridescence. Also, the high *Pe* of our system and the bidispersity suggest random

packing, as we mentioned in Section 2.4. It is close-packed because the average height that a particle diffuses upwards in the experimental conditions is lower than 2 μm, as we saw in Section 4.8.

- The sediment arranges into two distinct layers of constant composition. In the experiments, the sediment seemed to arrange into two distinct layers. Later in Section 5.3.5 we will discuss the assumption of constant composition by comparison with experimental results. A more accurate prediction should not include limitations to the number of layers in the sediment.
- The interphase boundary between the two phases of the sediment is sharp, without a transition region between the two phases. We will contrast this assumption with experimental results later in Section 5.3.5.
- The supernatant fluid on top of the sediment is free of particles. This assumption was verified experimentally for every experiment except for the case of nanoparticles. Again, the low diffusion height corroborates this assumption.

5.3.4 Modeling

5.3.4.1 Degrees of Freedom

The sediment is considered to arrange thermodynamically to a minimum free energy configuration. At that point the two phases should have reached a thermodynamic equilibrium. We can analyze the degrees of freedom of a system in thermodynamic equilibrium by using Gibb's phase rule[7]:

$$F = C - P + 2 \qquad (5.8)$$

Where F represents the degrees of freedom in the system, in other words the number of intensive properties which are independent of other intensive variables. *C* is the number of components and *P* the number of phases in thermodynamic equilibrium with each other. Let us consider our particular case:

- $C = 3$. We are dealing with three components, typically: large colloidal particles, small colloidal particles, and water.
- $P = 3$. We are considering the system divided into 3 phases: two for the sediment, upper and lower phase, and the supernatant.

Therefore, the degrees of freedom in our system is $F = 3 - 3 + 2 = 2$. However, as we mention in the previous section, temperature and pressure are given for the system. We are considering atmospheric pressure and a temperature of 20 ºC. Under those conditions, all the variables are specified and there is only one possible state for the equilibrium.

5.3.4.2 Known variables

Before starting the modeling work, let us specify which are the known variables in the system:

- a_L and a_S: particle radius of the large and small particles respectively
- T and P: temperature and pressure in the system respectively
- ρ_{LP} and ρ_{SP}: particle density of the large and small particles respectively
- ρ_f: density of the fluid
- m_L and m_S: total masses of the large and small particles respectively

- m_f: total mass of the fluid.
- κ^{-1}: Debye length around the particles
- g: gravitational/centrifugal acceleration
- A_S: cross sectional area of the sediment
- h_0 : total height of the vessel

5.3.4.3 Goal variables

Our goal is to know the following parameters that make the potential energy of the system be in a minimum state:

- f_{S1}, f_{S2}: volume fraction of the small particles in phase 1 and 2 respectively, relative to the total volume of particles in each phase.
- $h1$, $h2$, $h3$: height of the bottom layer of the sediment, the top layer of the sediment and height of the supernatant respectively.

5.3.4.4 Soft sphere parameters

We are considering soft-sphere interactions. Let us calculate the soft sphere radii using eq. 5.4 and the soft sphere densities ρ_L and ρ_S using eq. 5.6. We are going to assume that the soft sphere radius is given by the particle radius plus one time the Debye length. Therefore, the radius ratio r_r of our system is given by:

$$r_r = \frac{a_L + \kappa^{-1}}{a_S + \kappa^{-1}} \tag{5.9}$$

5.3.4.5 Mass balances

Since the whole system is closed and there is no generation or creation, the total mass of each of the components in the system has to remain unchanged.

$$m_L = A_S h_1 \phi_1 (1 - f_{S1}) \rho_{LP} + A_S h_2 \phi_2 (1 - f_{S2}) \rho_{LP} \quad (5.10)$$

$$m_S = A_S h_1 \phi_1 f_{S1} \rho_{SP} + A_S h_2 \phi_2 f_{S2} \rho_{SP} \quad (5.11)$$

$$m_f = A_S h_1 (1 - \phi_1) + A_S h_2 (1 - \phi_2) + A_S h_3 \quad (5.12)$$

Where ϕ_1 and ϕ_2 are the volume fraction of particles in the two layers of the sediment. We are assuming random close packing for ϕ_1 and ϕ_2. The actual values of packing are calculated by extrapolating the packing fraction data of reference 6 using the software Wolfram Mathematica 7. Equations 5.10, 5.11 and 5.12 can be reordered to express each of the heights as:

$$h_1 = \frac{h_0 \phi_0}{\phi_1} \times \frac{(f_{S0} - f_{S2})}{(f_{S1} - f_{S2})} \quad (5.13)$$

$$h_2 = \frac{h_0 \phi_0}{\phi_2} \times \frac{(f_{S0} - f_{S1})}{(f_{S2} - f_{S1})} \quad (5.14)$$

$$h_3 = h_0 (1 - \phi_0) - h_1 (1 - \phi_1) + h_2 (1 - \phi_2) \quad (5.15)$$

Where ϕ_0 is the total volume fraction of particles and f_{S0} is the total volume fraction of small particles relative to the total volume fraction of particles. Those values can be calculated from the total masses of particles and fluid.

5.3.4.6 Gravitational potential energy

The gravitational potential energy of the system is given by an integral over the height of the vessel *x*. We will take the bottom of the vessel as the reference point:

$$E_P = \int_0^{h_0} mgdx \tag{5.16}$$

Where *m* is the mass of the system. Since our system can be divided into three different phases, we can split the integral into three:

$$E_P = \int_0^{h_1} m_1 gdx + \int_{h_1}^{h_1+h_2} m_2 gdx + \int_{h_1+h_2}^{h_1+h_2+h_3} m_3 gdx \tag{5.17}$$

To calculate the mass of each phase m_i we are going to consider the volume of each section and its buoyant density:

$$m_i = A_s x(\rho_i - \rho) \tag{5.18}$$

Where ρ_i represents the effective densities of each phase. Notice that in the case of the supernatant the density of the phase and the density of the fluid are the same. As a consequence, the third integral is equal to zero. The effective densities of the two phases in the sediment can be calculated using eq. 5.7 as:

$$\rho_i \approx \phi_i \ f_{Si}\rho_S + \phi_i (1 - f_{Si})\rho_L + (1 - \phi_i)\rho \tag{5.19}$$

Using these expressions, eq. 5.15 is transformed into:

$$E_P = A_s g\left[\int_0^{h_1} \phi_1 \mathrm{P}_1 x dx + \int_{h_1}^{h_1+h_2} \phi_2 \mathrm{P}_2 x dx\right] \tag{5.20a}$$

$$\mathrm{P}_1 = (\rho_L - \rho_f) + f_{S1}(\rho_S - \rho_L) \tag{5.20b}$$

$$\mathrm{P}_2 = (\rho_L - \rho_f) + f_{S2}(\rho_S - \rho_L) \tag{5.20c}$$

Solving the integral gives us the following result:

$$E_P = \frac{A_s g}{2}\left[\phi_1 \mathrm{P}_1 h_1^2 + \phi_2 \mathrm{P}_2 (h_2^2 + 2h_2 h_1)\right] \tag{5.21}$$

The minimization of the potential energy was performed using the software Wolfram Mathematica 7. The code is included in Appendix B.

5.3.4.7 Entropy of mixing

Our objective is to estimate the entropy due to particle mixing in the sediment. At this point we are going to neglect the existence of water in the mixing. Therefore, we will only consider two different species mixing in the vessel: large and small particles. In the case of an ideal solution, the entropy of mixing can be calculated as:

$$\Delta S_{mix} = -nR\left(x_L \ln x_L + x_S \ln x_S\right) \tag{5.22}$$

Where n is the total number of particles in the mixture, x_L and x_S are the number fractions of the large and small particles respectively, and R is the ideal gas constant. The contribution of the entropy of mixing to the free energy in the case of an ideal solution (no enthalpy of mixing) is:

$$\Delta G_{mix} = nRT\left(x_L \ln x_L + x_S \ln x_S\right) \tag{5.23}$$

We can calculate the free energy of mixing for both phases of the sediment. In the experimental conditions that we are considering (micron size colloidal particles and a sediment height in the order of cm), ΔG_{mix} is 3 or 4 order of magnitudes lower than the gravitational potential energy (see Appendix B). As a consequence, the contribution of the entropy of mixing can be neglected compared to the gravitational potential energy.

5.3.4.8 Interparticle forces

Another contribution to the total energy is given by the interparticle forces within colloids. An exact calculation of the multiple interactions within the colloidal particles in the sediment is rather challenging. The various possibilities of multibody interactions and the particular characteristics of each particle enormously increase the complexity of the system. Let us make an estimate of this energy to have an idea of its order of magnitude:

- In the case of a monodisperse sample of spheres, the number of particle contacts for each particle is roughly 6 (see Section 2.3). Let us consider that each particle interacts with other 6 particles.
- The typical interaction energies between colloidal particles are in the order of a few kT. Let us consider that each particle-particle interaction is $2kT$ (from the DLVO interparticle interaction).

In our system of colloidal particles, this interaction energy is 3 orders of magnitude lower than the gravitational potential energy (see Appendix B). Therefore, it can be neglected in the calculation of the minimum energy configuration.

5.3.5 Results

The minimum potential energy model has been tested, trying to reproduce some of the experiments in Chapter 4. First, we have tried to use the model to analyze the case of silica and PSL. We have set the initial conditions to have a dispersion of silica and

PSL at 0.01 volume fraction, producing a sediment of 3cm. The predicted composition and the experimental results (Appendix A) are in good agreement (see Table 5.1).

Table 5.1 Comparison between experimental data and model predictions for silica-PSL mixtures

Particles	g Force	Relative Volume	Top Layer Experimental	Top Layer Model	Bottom Layer Experimental	Bottom Layer Model
3 μm Sulfate PSL - 3 μm Silica	1	1:1	100% PSL 0% Silica	100% PSL 0% Silica	0% PSL 100% Silica	4×10^{-6}% PSL ≈ 100% Silica
3 μm Sulfate PSL - 3 μm Silica	1000	1:1	100% PSL 0% Silica	100% PSL 0% Silica	0% PSL 100% Silica	2×10^{-7}% PSL ≈ 100% Silica
3 μm Sulfate PSL - 3 μm Silica	1	9:1	100% PSL 0% Silica	99.99% PSL 0.01% Silica	0% PSL 100% Silica	0.02% PSL 99.98% Silica

The experiment of 4.9 μm sulfate PSL and 150 nm gold could not be tested because we do not have packing fraction data for such an extreme radius ratio. The model can also be used to predict the phase compositions of sediments produced by particles made of the same material but with different sizes (see Table 5.2). See appendix A for the experimental data.

Table 5.2 Comparison between experimental data and model predictions for PSL mixtures of different sizes

Particles	g Force	Relative Volume	Top Layer Experimental	Top Layer Model	Bottom Layer Experimental	Bottom Layer Model
1 μm Sulfate PSL - 2 μm Sulfate PSL	1	1:1	100% 1 μm 0% 2 μm	99.9% 1 μm 0% 2 μm	23.2% 1 μm 76.8% 2 μm	21.1% 1 μm 78.9% 2 μm
2 μm Sulfate PSL - 3 μm Sulfate PSL	1	1:1	100% 2 μm 0% 3 μm	99.3% 2 μm 0.7% 3 μm	32.7% 2 μm 67.3% 3 μm	25.5% 2 μm 74.5% 3 μm
2 μm Sulfate PSL - 4 μm Sulfate PSL	1	1:1	100% 2 μm 0% 4 μm	99.3% 2 μm 0.07% 4 μm	24.7% 2 μm 75.3% 4 μm	27.1% 2 μm 71.9% 4 μm

3 μm Sulfate PSL - 4 μm Sulfate PSL	1	1:1	100% 3 μm 0% 4 μm	99.3% 3 μm 0.07% 4 μm	36.9% 3 μm 63.1% 4 μm	30.0% 3 μm 70.0% 4 μm
3 μm Sulfate PSL - 4.9 μm Sulfate PSL	1	1:1	100% 3 μm 0% 4.9 μm	93.3% 3 μm 6.7% 4.9μm	22.1% 3 μm 67.9% 4.9 μm	29.1% 3 μm 70.9% 4.9 μm

As we mentioned in Chapter 4, the recovery method does not provide a perfect recovery of the bottom layer. The experimental and predicted results show some number discrepancy. The model provides an approximate idea of the composition of each layer. Improving the analysis of the sediment composition is critical to test the limitations of the model. We also wanted a clearer microscopic examination of the sedimentation process and resulting layer compositions to compare with the model predictions. Thus, we ran an experiment using 4.0 μm red fluorescent and 2.0 μm yellow-green fluorescent sulfate PSL particles. We prepared a sample with a 1:1 volume ratio of the particles and allowed them to settle in a capillary tube slightly slanted to one side for 3 weeks. Since the capillary tube is tilted, it was possible to take images of the different layers of the sediment using confocal microscopy (see Section 3.6). The experimental results showed that the top of the sediment is composed exclusively of small particles (Figure 5.5A), then there is a small transition region of around 100 μm (Figure 5.5B). Finally, there is a lower layer with roughly a uniform composition of mixed particles (Figure 5.5C&D).

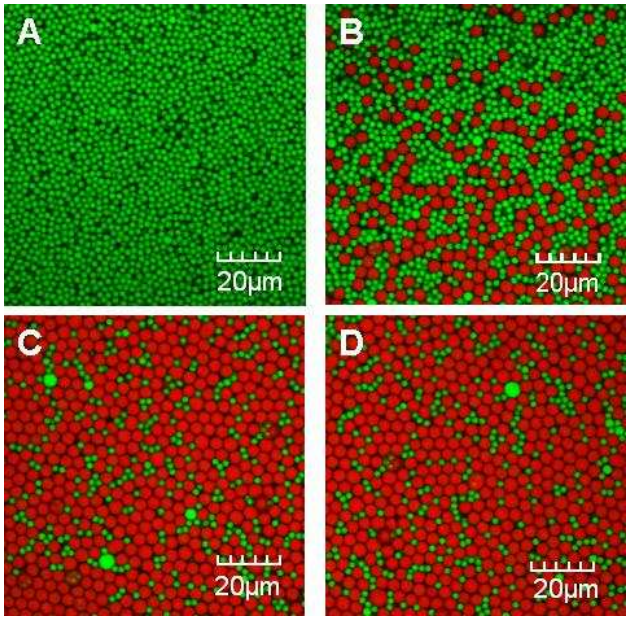

Figure 5.5 Confocal microscopy images of a sediment formed by an initial mixture of 1:1 volume ratio of 4 red fluorescence and 2 µm yellow-green fluorescence PSL particles. **A** Top layer of the sediment composed exclusively by small particles. **B** Transition zone of the sediment. **C** Mixture present at the lower layers of the sediment. **D** Mixture present at the bottom of the sediment.

Let us compare the confocal observation of the sediment in Figure 5.5 with the model prediction and assumptions. The transition zone in Fig. 5.5B is on the order of 100 µm. In the model, we consider this transition zone nonexistent. A transition zone in the order of microns for a sediment in the order of cm is negligible. We also considered that the sediment was arranged into two phases of constant composition. The composition of the upper layer revealed to be constant and pure in 2 µm colloids. The images of Figure 5.5C and 5.5D correspond to the bottom layer of the sediment. By using confocal microscopy it was possible to image the particles at the wall of the capillary. However, it

was impossible to get images deep in the capillary because the high packing fraction of the particles did not allow the penetration of light. As consequence, we could only get a bidimensional image of the sediment. Although we cannot get a value of its packing fraction, we can get a value of the surface coverage fraction. The surface coverage from Figure 5.5C was 0.840 ± 0.014, while of the one for Figure 5.5D was 0.868 ± 0.013. Those values are statistically different enough to suggest that the composition of the bottom layer is not completely constant. However, since the variation is in the order of 3%, the assumption of constant composition can be used for a simplified model.

5.3.6 The limitation: particle aggregation due to gravity

As we observed experimentally in Section 4.5, gravity can influence the sediment reordering since the particles may aggregate. In this section, we are going to do an analysis of the gravitational effects in the colloidal forces acting on the particles.

Let us imagine two colloidal particles at the bottom of the vessel, one on top of the other. If both particles are charged, and the surface potential is high enough, the electrostatic repulsion will prevent them from aggregating. There are two forces that are trying to pull both particles together: van der Waals forces and gravity. If one particle is on top of the other, gravity is acting on the particle at the top, trying to lower the particle height and, as a consequence, the interparticle separation. If we only have two colloidal particles, then the effect of gravity is negligible compared to the electrostatic and van der Waals forces. Now let us consider a particle that has 20 particles on top. The second particle will feel the weight of the other 19 particles in the same way that we feel the weight of air molecules on top of us. This will increase the force that pulls the two

particles closest to the bottom together. If the gravitational force is increased, then this effect will be even more important.

The influence of gravity in particle aggregation can be predicted qualitatively using a modified version of the DLVO theory. DLVO theory calculates the interaction energy between two particles just by adding together the electrostatic repulsion and the van der Waals attraction between the particles[8] (eq. 5.24).

$$\Phi \approx \Phi_{DLVO} = \Phi_{ES} + \Phi_{VDW} \tag{5.24}$$

To calculate the electrostatic interaction energy many equations have been derived. It is important to know the assumptions made to obtain each expression. In our case we are dealing with spherical particles with high surface potentials ($\psi_0 > |50|$ mV). No analytical solution is available for this case, but Ohshima et al.[9] and Sader et al.[10] provided different ways to predict the electrostatic interaction. We are going to use the results derived by Sader et al.:

$$\Phi_{ES} = 4\pi\varepsilon\left(\frac{kT}{e}\right)^2 Y^2 \frac{a^2}{2a+\delta}\ln\left(1+e^{-\kappa\delta}\right) \tag{5.25a}$$

$$Y = 4e^{\kappa\delta/2}\tanh^{-1}\left[e^{-\kappa\delta/2}\tanh\left(\frac{Ze\psi_s}{4kT}\right)\right] \tag{5.26b}$$

Where δ is the interparticle distance and ψ_S is the surface potential. In the case of a Z:Z electrolyte, the Debye length is calculated with equation 5.1.

Also, some models have been derived to predict the van der Waals attraction between colloidal particles. The prediction of the quantum mechanics in this interaction is not an easy task. Hamaker gave a relatively simple result to this problem that we are going to use for our system.

$$\Phi_{VDW} = -\frac{A}{12}\left(\frac{y}{x^2+xy+x}+\frac{y}{x^2+xy+x+y}+2\ln\frac{x^2+xy+x}{x^2+xy+x+y}\right) \quad (5.27)$$

Being $x = \delta/2a_1$ and $y = a_1/a_2$, where a_1 and a_2 are the radius of the particles 1 and 2 respectively, and A is the Hamaker constant. For a PSL-PSL interaction in water, $A = 1.4\times10^{-20}$ J.

We are going to add the influence of gravity to the electrostatic and the van der Waals interaction. Let us go back to case of two particles, one of top of the other. We will consider that the particle at the bottom has its position fixed. For example, the particle is in contact with the bottom of the vessel. Then, we consider that gravity is acting on the particle on top trying to pull it down. Next, we are going to estimate the gravitational energy of the second particle. First, we need to define a reference point for the energy: we will assume that the potential energy of the particle on top is zero when both particles are touching each other. At that point the particle separation distance is $\delta = 0$ (notice that this is different from the electrostatic and van der Waals interactions where the zero energy is defined at particle separation distance $\delta = \infty$). Then, what is the energy cost of lifting the particle on top from the contact point to a distance δ?:

$$\Phi_{grav} = \frac{4}{3}\pi a^3\left(\rho_p - \rho\right)g\delta \quad (5.28)$$

This equation is valid for one sphere on top of another one, but what about the case of a column of spheres on top of one particle? What is the energy cost of lifting the whole column on top from the contact point to a distance δ? The potential energy of the whole column E^0_{grav} is given by the sum of the potential energy of each particle.

$$E_{grav}^{0} = \sum_{i=1}^{N} \frac{4}{3} \pi a_i^3 \left(\rho_p - \rho\right) g h_i \tag{5.29}$$

Where a_i and h_i are the radius and the height of each particle in the column respectively. If we pull the column up a height δ, all the particles in the column will be elevated a distance δ. As a consequence, the new potential energy of the system E_{grav}^{δ} will be given by:

$$E_{grav}^{\delta} = \sum_{i=1}^{N} \frac{4}{3} \pi a_i^3 \left(\rho_p - \rho\right) g \left(h_i + \delta\right) \tag{5.30}$$

Thus, the energy required to pull the whole column up a height δ will be given by the energy difference between the final and initial states.

$$\Phi_{grav} = E_{grav}^{\delta} - E_{grav}^{0} = \sum_{i=1}^{N} \frac{4}{3} \pi a_i^3 \left(\rho_p - \rho\right) g \delta \tag{5.31}$$

If we consider that all N particles in the column are identical and they have a particle radius a, then the potential energy required can be rewritten as:

$$\Phi_{grav} = N \frac{4}{3} \pi a^3 \left(\rho_p - \rho\right) g \delta \tag{5.32}$$

To calculate the total interaction energy, also considering the contribution of the potential energy, we are going to add Φ_{grav} to the DLVO equation (5.24).

Let us calculate the total energy for two 2 μm PSL particles with a surface potential of -70mV in DI water at 293 K. We are going to consider three cases: two isolated particles (one particle on top of the other) at 1g, a column of 5 particles on top of one particle at 1000g, and a column of 20 particles on top of one particle at 1000g (Figure 5.6).

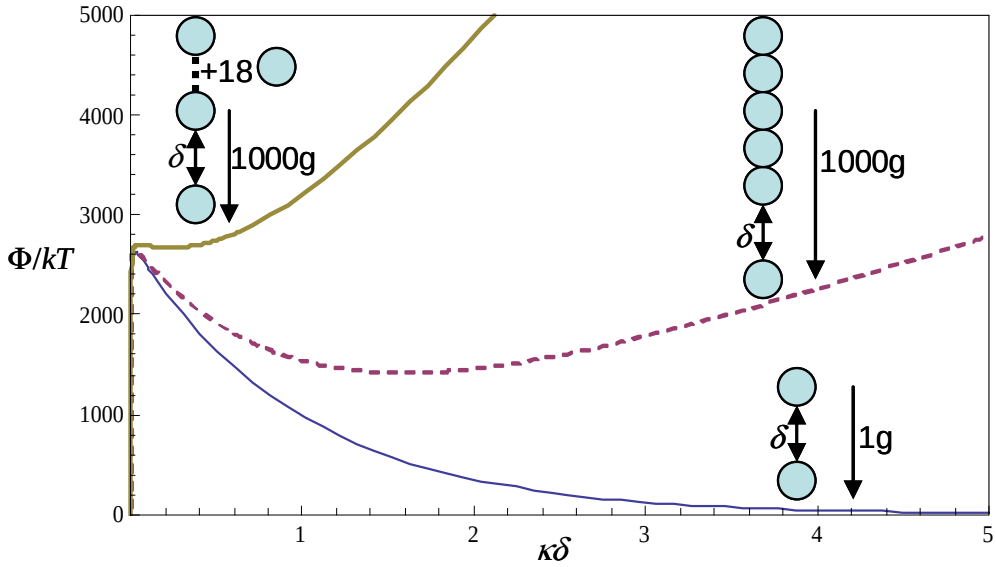

Figure 5.6 Interaction energy between particles under the action of gravity. (——) Interaction energy for two 2 μm PSL particles placed one on top of the other in water at 1g. (– – –) Interaction energy for a 2 μm PSL particle and a column of 5 similar particles in water at 1000g. (——) Interaction energy for a 2 μm PSL particle and a column of 20 similar particles in water at 1000g.

Let us analyze the results in Figure 5.6. First we have to notice that the energies involved in this system are really high for colloidal interactions (thousands of *kT*). This situation is created by the high surface potentials on the particles and the high gravitational acceleration used. In the case of two spheres at 1g, the interaction energy increases as the separation distance becomes smaller. That means that as we approach both particles, the electrostatic repulsion between them rises and the amount of energy required to bring them together increases. On the other hand, in the case of the column of spheres on top of one particle, it requires a lot of energy to have the column at a high altitude. Actually, the column will move from higher altitudes down to a point where the

energy finds a minimum. As it can be seen from Figure 5.6, in the case of the column of 5 particles, the minimum is located at $\kappa\delta \approx 1.3$. However, in the case of the column of 20 particles, the minimum is located at separation $\kappa\delta \approx 0$. At this point the column and the particle will aggregate together.

The implications of aggregation under high centrifugal forces and/or high sediment heights (a column with a large number of particles on top) must be taken into account when predicting the sediment formation.

5.4 Hypothesis of how particles can reach the minimum energy configuration

While we have not evaluated the detailed transport dynamics that affect the final sediment compositions, although it might be analyzed by a Stokesian Dynamics simulation[11], we expect that the soft sphere state of our particles enables sediment layering. As we observed in Section 4.7, diffusion coefficients for interacting, repulsive spheres are effectively not zero. We expect that particles with larger-magnitude surface potentials will remain mobile at higher volume fractions due to their increased repulsion. Non-zero diffusion coefficients perhaps allow for our sediments to rearrange themselves into the predicted thermodynamically favorable configuration. If our particles were glassy, rather than showing mobility as seen in Figure 4.9, this re-arrangement would not occur, and the particles would freeze into a non-equilibrium configuration. Actually this freezing behavior was observed by Royall et al.[12] working with hard spheres.

Hydrodynamic effects may also aide the system in reaching the equilibrium configuration. It is likely that at the solution-sediment interface, backflow caused by larger or denser settling particles sweeps less dense particles upward. We also expect that a type of "coalescence" occurs, even in bulk solution, such that if by Brownian motion 5 or 10 particles happen to approach each other at some instant – and this will happen statistically – this local region has a higher effective density and begins to settle more quickly. The coalescence might provide an additional path toward separation, even in the bulk fluid, by allowing the particles to organize into locally minimum energy configurations before they have finished settling. Additionally, in concentrated particle systems, the difference in settling rate between particles and their counter-ions can induce an electric field that can cause segregation during the sedimentation process, based on particle charge-to-mass ratio[13]. This effect can cause deviations in settling even at low volume fractions[14] of 10^{-5}.

Convection currents have also been observed during the sediment formation. In Figure 5.7 we first produced a sediment of 3 μm red sulfate PSL particles settling at 1g. Then we settled 2 μm green sulfate PSL on top of them. As time passed, it can be seen how the 2 μm green particles penetrated into the sediment on one side, while the 3 μm red particles rose on the other side. How is this possible? When we first produced a sediment with 3 μm particles, the packing fraction corresponded to a monodisperse distribution. As the 2 μm particles reached the top of this sediment, they started to mix with the 3 μm particles. That mixture was on top of a monodisperse distribution of spheres, but the effective density of the mixture is higher. This is an unstable situation, since the heavier

phase is on top of the lighter one. As a result, the mixture tended to fall while the monodisperse 3 μm particles tended to rise, creating a convective movement.

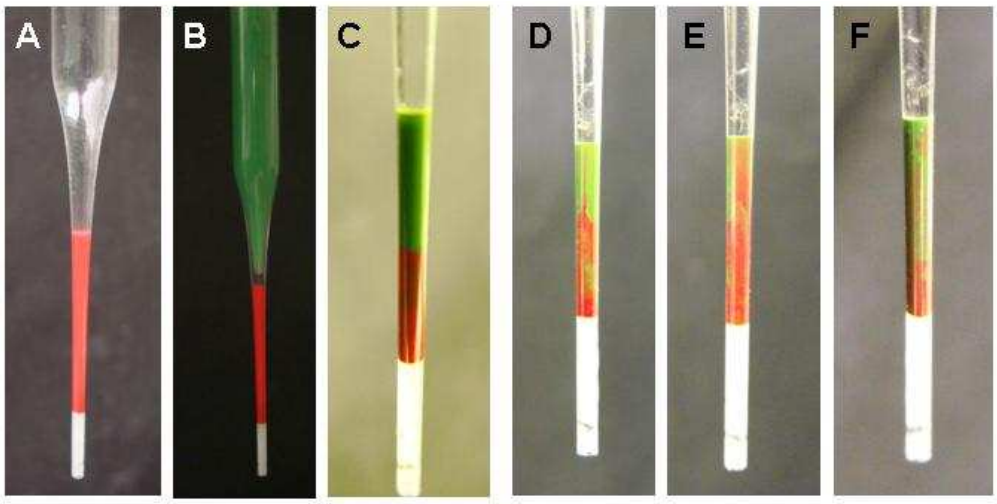

Figure 5.7 Convection currents observed during the sediment formation. **A** Sediment produced by 3 μm red sulfate PSL particles settling at 1g. **B** Addition of 2 μm green sulfate PSL particles on top of the sediment in **A** at 1g. **C** The sediment after 7 days. **D** The sediment after 22 days. **E** The sediment after 27 days. **F** The sediment after 39 days.

5.5 References

[1] Hunter, R.J. "Zeta Potential in Colloid Science: Principles and Applications." (Academic. Press, New York, 1981.).

[2] Behrens, S.H., Grier, D.G. *J. Chem. Phys.* **115**, 6716 (2001).

[3] Handley, D.A. "Colloidal Gold Principles, Methods and Applications." Academic Press (Academic Press , San Diego, 1989).

[4] Russel, W.B., Saville, D.A., Schowalter, W.R. "Colloidal Dispersions" (Cambridge Univ. Press, Cambridge, 1999).

[5] Velegol, D. "Colloidal Assemblies. From physical concepts to useful assemblies… quickly." To be published.

[6] Lochmann, K., Oger, L., Stoyan, D. *Solid State Sci.* **8**, 1397-1413 (2006).

[7] Gibbs, J.W. "Scientific Papers" (Dover, New York, 1961).

[8] Derjaguin, B. V., Landau, L. *Acta Physicochim. U.S.S.R.* **14**, 633 (1941); Verwey, E. J. W., Overbeek, J. Th. G. "Theory of the Stability of Lyophobic Col-loids" (Elsevier, Amsterdam, 1948).

[9] Ohshima, H., Healy, T.W., White, L.R, *J. Colloid Interface Sci*. **89**, 484-493 (1982).

[10] Sader, J. E., Carnie, S. L., Chan, D. Y. C. *J. Colloid Interface Sci*. **171**, 46-54 (1995).

[11] Brady, J. F., Bossis, G. Stokesian Dynamics *Ann. Rev. Fluid Mech.* **20**, 111-157 (1988).

[12] Royall, C.P., Vermolen, E.CM., van Blaaderen, A., Tanaka, H. *J. Phys.: Condens. Matter* **20**, 404225 (2008).

[13] Rasa, M., Philipse, A. P *Nature* **429**, 857-860 (2004).

[14] Wang, T., Li, H., Sheng, Y., Tsao, H. *J. Chem. Phys.* **129**, 204504 (2008).

Chapter 6

Conclusions and Future Work

6.1 Conclusions

The sediments produced by a dense suspension of bidisperse mixtures of micron-size charged spheres have been the central topic in this thesis. Spontaneous separation into two macroscopic layers was observed after sedimentation of the particles at *Pe* greater than unity. The layering behavior can be predicted by simply minimizing the potential energy of the system. This effect resulted in complete segregation for mixtures of particles made of different materials. In the case of bidisperse mixtures of particles with different sizes but made of different materials only partial segregation is achieved. The top layer consisted of pure small particles, while the bottom layer had a mixture containing a high proportion of big particles. Although the technology is not fully developed yet, the science of these results can be applied to sort high throughput of colloidal particles by size or density. It has also been shown that the influence of gravity on particle aggregation can influence the sediment formation.

In principle, this theory could be applied to predict final sediment layer compositions for any multi-component mixture of particles in which the particles remain mobile. Indeed, we performed one experiment with 5 different particles at 1000g, each having a different size or density, and we obtained a reasonable sorting for all of these, almost like a fractionating distillation column (Figure 6.1). On the other hand, few

results exist – either from modeling or experiments – for the packing fractions of multi-component mixtures of spherical particles, and even less so for mixtures of say singlet and doublet particles. Such studies require great care.

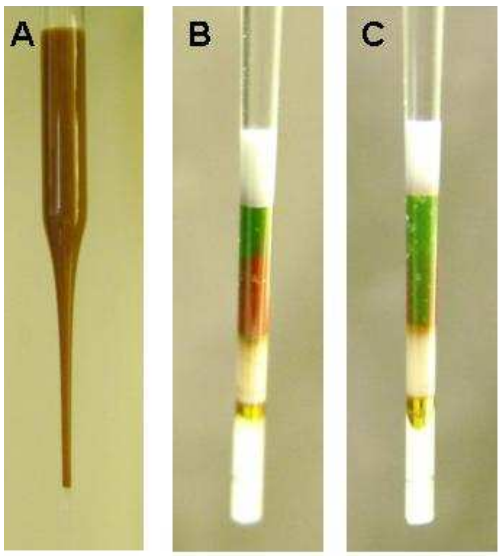

Figure 6.1 Layers of sorted particles. **A** Original mixture of 150 nm gold, 3 μm white silica, 3 μm red sulfate PSL, 2 μm green sulfate PSL and 0.99 μm sulfate PSL at 0.01 volume fraction. **B** Front view of the 5 layer cake after centrifugation at 1000g for 30 minutes. The white region at the bottom is wax sealing the glass capillary. **C** Back view of the 5 layer cake after centrifugation at 1000g for 30 minutes.

Although the motivation of this work was to develop a sorting procedure for colloidal assemblies, the implications of this research may impact other disciplines. The basics of the layering behavior could be used to accomplish the separation of mixtures with cell organelles or even proteins with a much higher throughput and reliability. Furthermore, shipment of colloidal or emulsion products by truck or train might be accomplished without unwanted de-mixing due to vibrations. In fact, this science can be

applied not only to technological processes, but to understand natural phenomena. Data for geological or environmental layers of silt or clay layering might be interpreted differently.

This work has been submitted for publication to *Nature Materials* on May 4th, 2010 under the title "Sediments of Soft Spheres Arranged by Effective Density".

6.2 Comparison with possible similar systems

Having a mobile sediment composed of particles with two different sizes may bring the Brazil Nut Problem to the reader's mind. In fact, this phenomenon has some similarities with our problem, but some subtle differences as well that are important to explain the particular outcomes of each situation. The so called Brazil Nut Problem (BNP) consists of shaking a container with rigid particles of two different sizes. It has been found that under this situation the large particles merge to the top of the particle container.[1] A Reverse Brazil Nut Problem, where the big particles sink to the bottom, has been addressed by changing the density ratio of the particles.[2] The key difference with our system lays in the fact that the final configuration of the sediment in the BNP is a metastable state. Rosato et al.[3] pointed that "At equilibrium, if a large particle is placed in a container filled with smaller particles of equal or lesser density the large particle will be on the bottom in order to minimize the potential energy". We have also discovered that in the case of a collection of large particles in a container with small particles, the minimum potential energy is given by a mixture due to packing effects. Rosato et al. also pointed that in the case of BNP the fact that the system "proceed upon shaking to a nonequilibrium metastable state is rather surprising". They used an adaptation of the

Monte Carlo method to study the dynamics of size segregation in the BNP and in the equilibrium (see Figure 6.2). Notice that in the case of the minimum potential energy (Figure 6.2A) a mixture of large and small particles is actually found at the bottom.

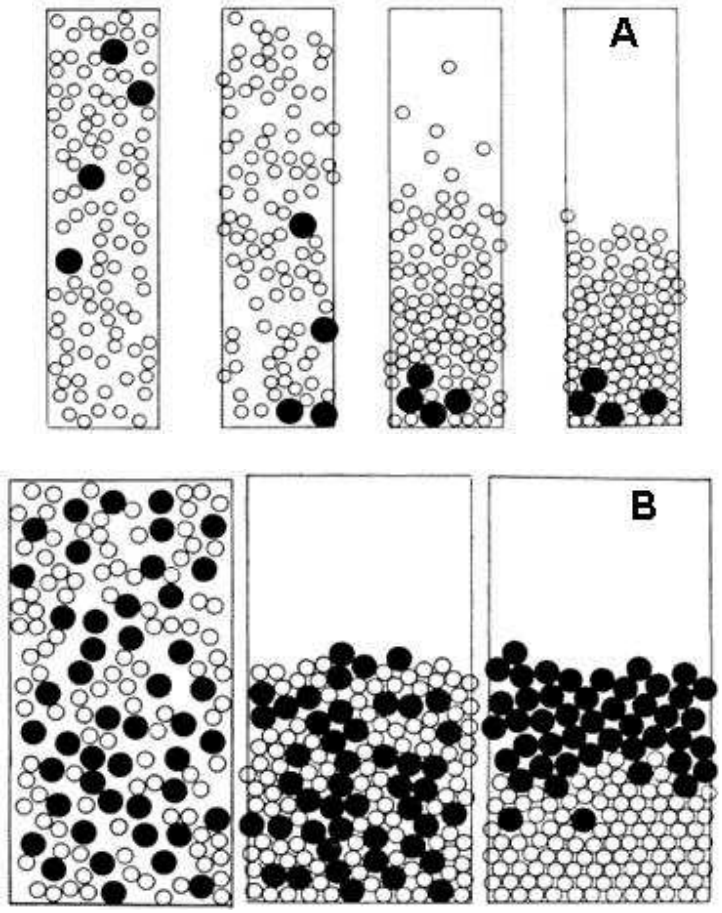

Figure 6.2 Monte Carlo simulations of particle segregation taken from reference 3. **A** Time frames of the simulation where the system is allowed to reach an equilibrium configuration. **B** Times of the BNP simulation.

The reason why our system and the BNP evolve to different final states is a matter of the nature of the particles and the process itself. First, the BNP does not typically use a

"true temperature", but a biased temperature.[4] This occurs because while the particles are moved up at an arbitrary speed during shaking, depending upon the lift rate, they roughly fall with gravitational acceleration. Hence, this movement provides the particles an upward-downwards mobility. However, in the case of colloidal particles, Brownian motion is a 3-D movement. The lateral movement of the particles may allow others to go through different layers of the sediments as we saw in Figure 4.9. Second, since the particles settle in air at high Reynolds numbers, they roughly accelerate at the same rate. In contrast, the particles in our colloidal systems settle at terminal velocity, so that small particles settle more slowly than larger ones. Furthermore, the Stokes regime allows the colloidal particles to have long-range hydrodynamic interactions. As a consequence, the small particles can be swept up due to fluid movement created by the settling of the large ones.

Another comparison can be drawn with demixing in polymer mixtures.[5] However, it is important to notice that in such case the result of demixing is driven by the competition between entropy of mixing and interaction between polymer molecules. Gravity has only a small influence on the distribution. In our case the influence of gravity is dominant due to the length scale of the sediment.

6.3 Future work

6.3.1 Application to sorting

The results presented in this thesis are promising showing that these principles can be applied to sorting of colloidal particles with different sizes or densities. However, the technology for the separation is not fully developed yet. Sedimentation of the

particles in a Pasteur pipette provides a good macroscopic observation of the sediment, but it is not suitable to sort kg/day of colloidal particles. Furthermore, the recovery method used to extract the different layers needs to be improved to reduce mixing between phases.

6.3.2 Application to sorting of colloidal assemblies

The application of these concepts to sorting of colloidal assemblies still requires some investigation in certain research areas. Packing fraction values of the desired assemblies to sort are required. The packing fraction of many complex assemblies is not known yet. In summer 2009, Kristi Ann Wegener and Tawana Hines studied the packing fraction of mixtures of singlets and doublets. They used plastic BB's glued together to represent doublets and single BB's as singlets (see Appendix C for a full description of methods and results). They found that the packing fraction of singlets is greater than the packing fraction of pure doublets or any singlet-doublet mixture (see Figure 6.3). The packing fraction value found for doublets were slightly lower than the one reported by Zou et al.[6] However, the important point is that the lower packing fraction of the doublets should provide a leading force for separation.

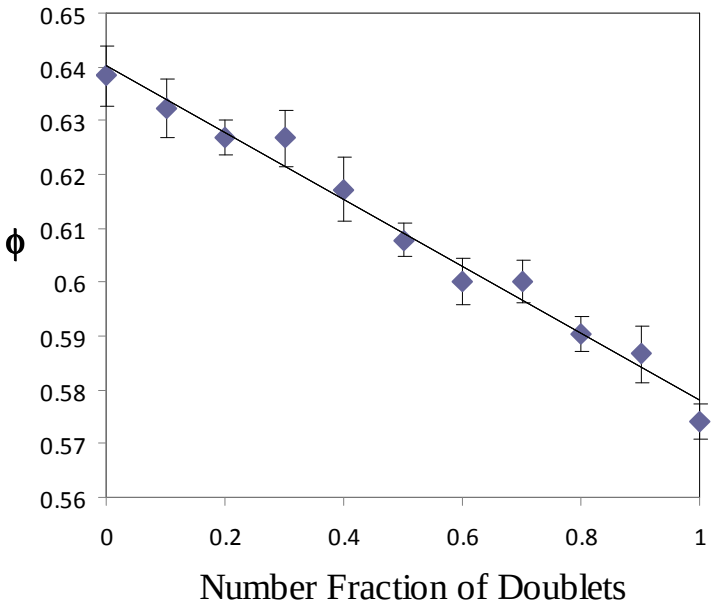

Figure 6.3 Packing fraction of mixtures of singlets and doublets. Data in Appendix C.

Although a perfect separation with the doublets on top is expected according to the minimum potential energy prediction, this result was not found in some preliminary experiments. The following points suppose a limitation to get the minimum potential energy state in the singlet-doublet case:

- Depending on the functionality, the doublets may suffer a dramatic decrease in the surface potential during the heating step of their fabrication.[7] This decrease on the surface potential reduces the electrostatic repulsion of the particles, thus increasing the effect of aggregation by gravity.
- Although the doublets should be on top, their settling velocity is higher than the singlets and in this case the sweeping of the fluid is pushing the singlets up.

Further experimentation is required to apply this methodology to the special case of singlets and doublets.

6.3.3 Improvement of the minimum potential energy model

The model of the minimum potential energy has an important assumption: the sediment arranges into two layers of constant composition. Slight changes in composition with height were found for the bottom layer in Figure 5.5. The model should include:

- Variation of the packing fraction with height in every layer.
- Variation of the interparticle distance with height. Due to the squeezing effect of gravity.
- Entropy of mixing including water. Flory-Huggins theory has been used for polymer solutions in order to account for the contributions of the polymer and the solvent. We may extrapolate that theory to apply it to mixtures of particles in water.

6.3.4 Study of the mechanisms influencing the sediment formation

The mechanisms of particle movement within the sediment need to be explored in detail to reveal the details of the sediment formation. Some of the possible mechanisms have been mentioned in Section 5.4. However, a deeper analysis of the fluid dynamics of the process would allow us to improve the sorting technology. Also, how the convection currents observed in Figure 5.7 developed and evolved is not yet well understood. Similar convection movement was found over long periods of time in certain sediments.

We experimentally followed the sediment evolution over long periods of time (weeks to months) and in some cases convection currents were observed. In the case of sediments of 2 and 3 μm sulfate PSL produced at 1g, convection currents were observed; specially in the case of a high sediment height (i.e. 3 cm, see Figure 6.4A). However, this result was never observed if the sediment was produced at 1000g (see Figure 6.4B) or in the case of silica and sulfate PSL mixtures (see Figure 6.4C).

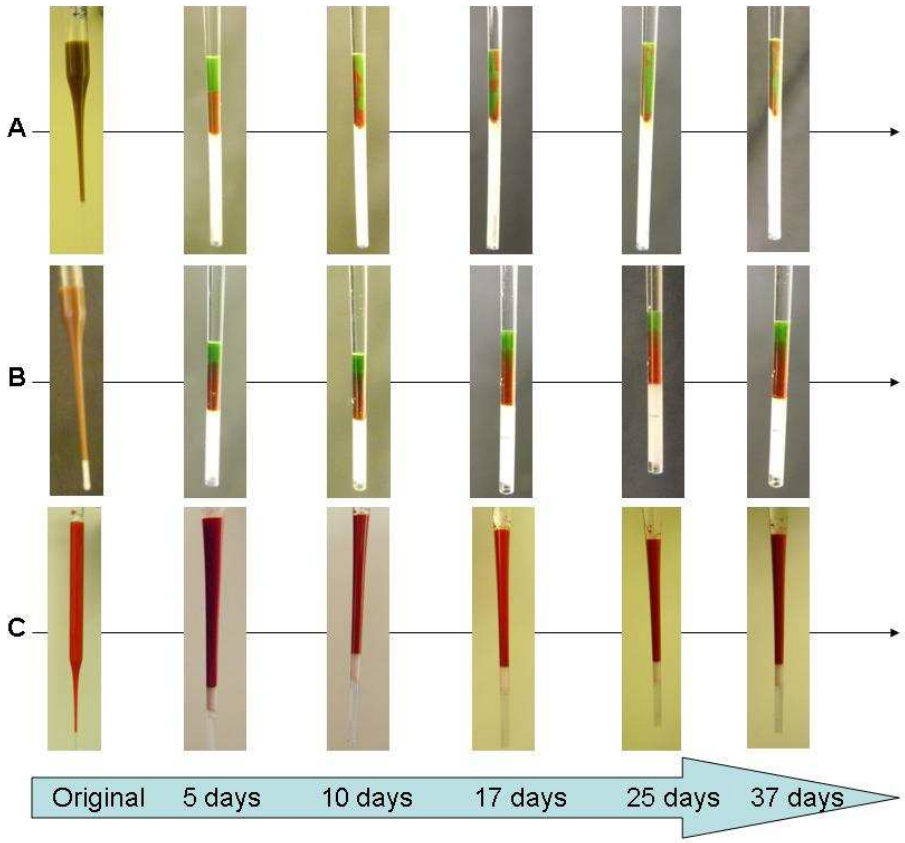

Figure 6.4 Time evolution of different sediments during 37 days. **A** Time evolution of a sediment produced by the settling at 1g of 2 and 3 μm sulfate PSL. Notice that convection currents developed, mixing the sediment. **B** Time evolution of a sediment produced by the settling at 1000g of 2 and 3 μm sulfate PSL. The sediment remained with no change after 3 months. **C** Time evolution of a sediment produced by the settling at 1g of 3 μm sulfate PSL and 3 μm silica. The sediment remained with no change after 3 months.

The nature of these convection currents is not completely well understood. Our current hypotheses in each case are the following:

- Figure 6.4A: Due to the elevated height of the sediment (3 cm), the particles at the bottom started to aggregate. The packing fraction of the aggregates was lower than the packing fraction of monodisperse spheres. The density of the packing at the bottom was lower than the density of the packing on top. As a consequence, convection currents were developed to restore the equilibrium.
- Figure 6.4B: The sediment was produced at a high centrifugal force and the sediment height is elevated. As a consequence, most of the sediment was aggregated and there was no mobility within it.
- Figure 6.4C: The silica particles at the bottom might start to aggregate. However, the high density of the silica was enough to overcome the decrease on the packing density due to the aggregation. The effective density of the bottom packing decreased but it was still higher than the density of PSL. As a consequence, no convection currents were produced.

The sediment with convection currents shown in Figure 6.4A was recovered after 37 days and analyzed in the microscope. Particle aggregates were found even in the top layers of the sediment (see Figure 6.5)

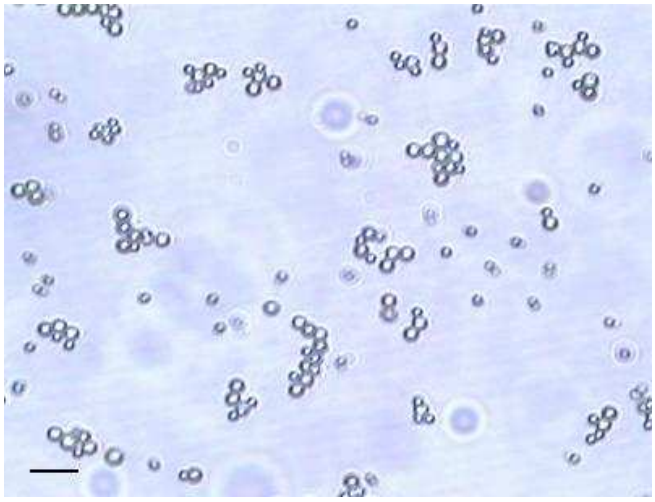

Figure 6.5 Optical microscopy image of the top layer of the sediment in Figure 6.4A after 37 days. During the recovery process the sediment was always kept in solution. Particle aggregates were found even after sonication for 10 minutes. The scale bar is 10 μm.

This phenomenon broke the layered structured of the sediment and it is a limitation for particle sorting. A deeper analysis must be performed to avoid such situations in a sorting process.

6.4 References

[1] Williams, J.C., *Powder Technol.* **15**, 245-251 (1976).

[2] Hong, D.C., Quinn, P.V., Luding, S. *Phys. Rev. Lett.* **86**, 3423-3426 (2001).

[3] Rosato, A., Strandburg, K. J., Prinz, F., Swendsen, R. H. *Phys. Rev. Lett.* **58**, 1038-1040 (1987).

[4] Quinn, P.V., Hong, D.C. *Phys. Rev. E* **62**, 8295-8298 (2000).

[5] Albertsson P. "Partition of Cell Particles and Macromolecules" (John Wiley & Sons, New York 1986).

[6] Zou, L. N., Cheng, X., Rivers, M.L., Jaeger, H. M., Nagel, S.R. *Science* **326**, 408-410 (2009).

[7] Yake, A. M., Panella, R. A., Snyder, C. E., Velegol, D. *Langmuir* **22**, 9135-9141 (2006).

Appendix A

Particle Recovery Images and Data

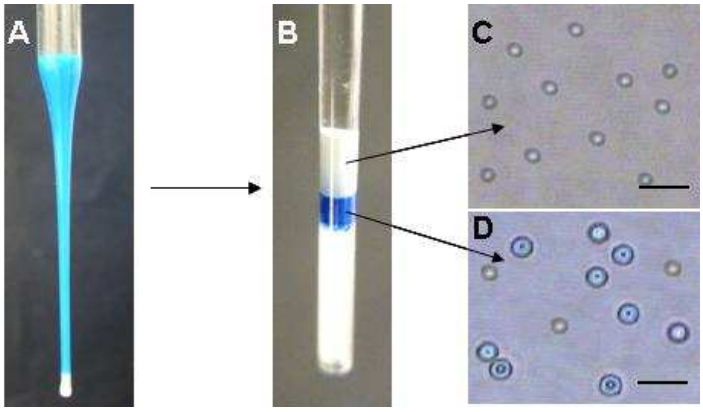

Figure A.1 Particle recovery of the sediment produced by sedimentation at 1g of a mixture of 2 and 1 μm PSL. All the scale bars at the bottom right of the images are 5 μm. **A** Mixture with equal volume of 2 μm blue and 1 μm white Sulfate PSL particles at an initial volume fraction 0.01. **B** Resulting sediment of **A** after sedimentation at normal gravity (1g) for 7 days. The white region at the bottom is wax sealing the glass capillary. **C** Optical microscopy image (100×) of the white region of the sediment in **B** after dilution with DI water. All the particles are 1 μm white PSL. **D** Optical microscopy image (100×) of the blue region of the sediment in **B** after dilution with DI water. The image shows a mixture of 2 and 1 μm particles.

Top Layer Composition: 100% 1 μm white PSL.

Bottom Layer Composition: 76.8% ± 4.9% 2 μm blue PSL

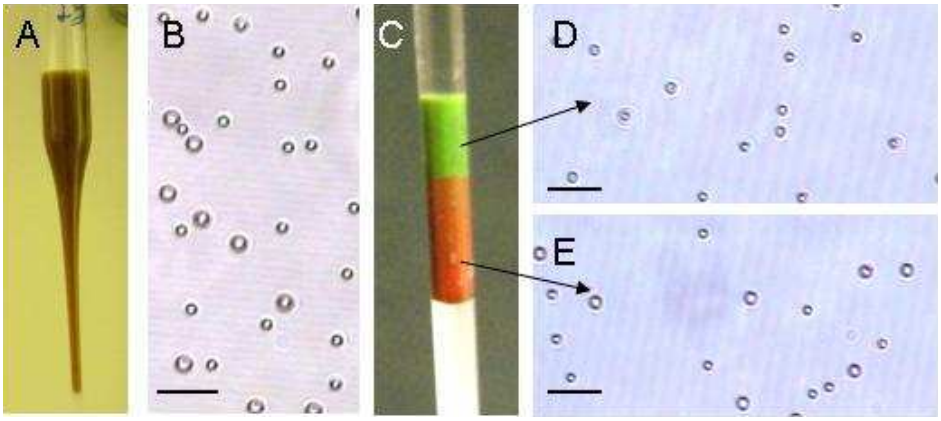

Figure A.2 Particle recovery of the sediment produced by sedimentation at 1g of a mixture of 2 and 3 μm polystyrene particles. All the scale bars at the bottom left of the images are 10 μm. **A** Mixture of 1:1 volume ratio of 2 μm green and 3 μm red sulfate-functionalized PSL particles at 0.01 volume fraction. **B** Optical microscopy image (40×) of the mixture in **A** after dilution to 10^{-4} volume fraction. **C** Resulting sediment of the mixture in **A** after sedimentation in gravity (1g) for 3 days. The white region at the bottom is wax sealing the glass capillary. **D** Optical microscopy image (40×) of the green region of the sediment in **C** after dilution with DI water. All the particles are 2 μm green PSL. **E** Optical microscopy image (40×) of the red region of the sediment in **C** after dilution with DI water. The image shows a mixture of 2 and 3 μm particles.

Top Layer Composition: 100% 2 μm green PSL.

Bottom Layer Composition: 67.3% ± 2.4% 3 μm red PSL

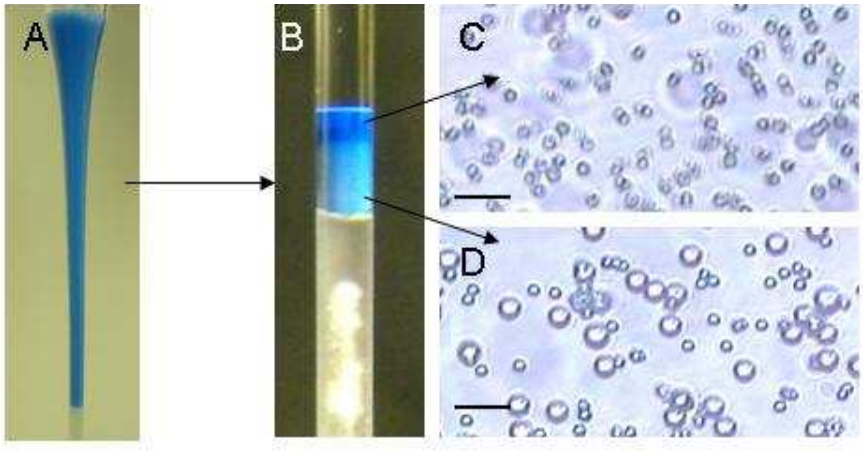

Figure A.3. Particle recovery of the sediment produced by sedimentation at 1g of a mixture of 2 and 4 μm polystyrene particles. All the scale bars at the bottom left of the images are 10 μm. **A** Mixture of 1:1 volume ratio of 2 μm blue and 4 μm white sulfate-functionalized PSL particles at 0.01 volume fraction. **B** Resulting sediment of the mixture in **A** after sedimentation in gravity (1g) for 5 days. The white region at the bottom is wax sealing the glass capillary. **C** Optical microscopy image (40×) of the dark blue region of the sediment in **B** after dilution with DI water. All the particles are 2 μm blue PSL. **D** Optical microscopy image (40×) of the light blue region of the sediment in **B** after dilution with DI water. The image shows a mixture of 2 and 4 μm particles.

Top Layer Composition: 100% 2 μm blue PSL.

Bottom Layer Composition: 75.3% ± 1.9% 4 μm white PSL

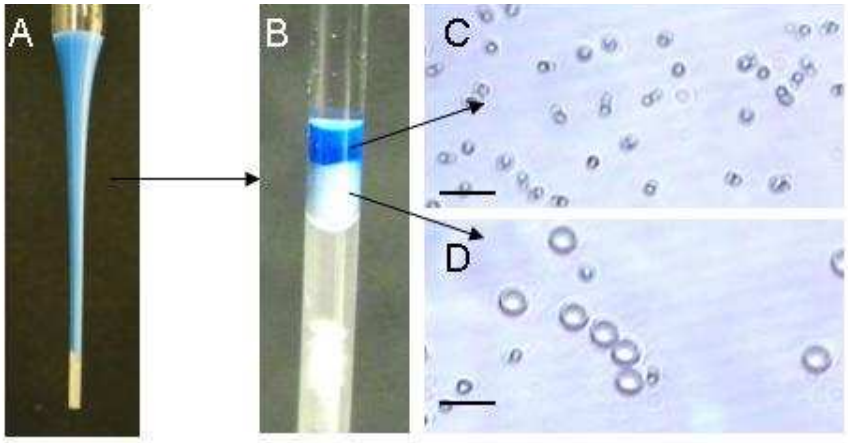

Figure A.4. Particle recovery of the sediment produced by sedimentation at 1g of a mixture of 2 and 4.9 μm polystyrene particles. All the scale bars at the bottom left of the images are 10 μm. **A** Mixture of 1:1 volume ratio of 2 μm blue and 4.9 μm red sulfate-functionalized PSL particles at 0.01 volume fraction. **B** Resulting sediment of the mixture in **A** after sedimentation in gravity (1g) for 5 days. The white region at the bottom is wax sealing the glass capillary. **C** Optical microscopy image (40×) of the blue region of the sediment in **B** after dilution with DI water. All the particles are 2 μm blue PSL. **D** Optical microscopy image (40×) of the white region of the sediment in **B** after dilution with DI water. The image shows a mixture of 2 and 4.9 μm particles.

Top Layer Composition: 100% 2 μm blue PSL.

Bottom Layer Composition: 93.7% ± 0.7% 4.9 μm white PSL

Comments: Aggregation was observed at the bottom of the sediment.

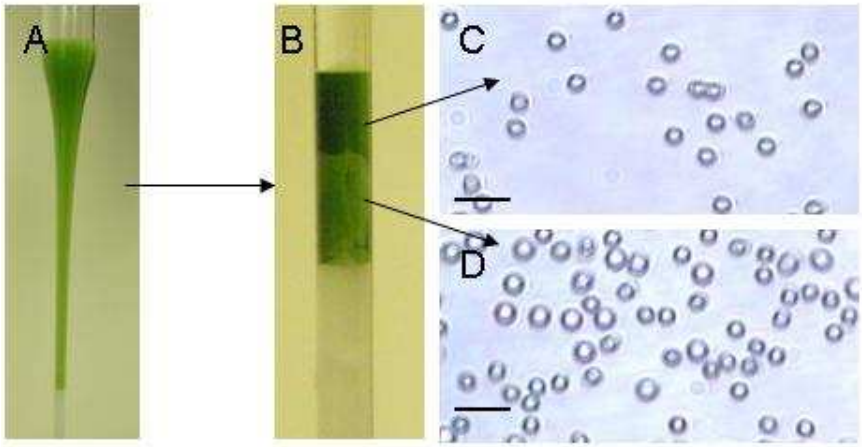

Figure A.5. Particle recovery of the sediment produced by sedimentation at 1g of a mixture of 3 and 4 μm polystyrene particles. All the scale bars at the bottom left of the images are 10 μm. **A** Mixture of 1:1 volume ratio of 3 μm green and 4 μm white sulfate-functionalized PSL particles at 0.01 volume fraction. **B** Resulting sediment of the mixture in **A** after sedimentation in gravity (1g) for 5 days. The white region at the bottom is wax sealing the glass capillary. **C** Optical microscopy image (40×) of the dark green region of the sediment in **B** after dilution with DI water. All the particles are 3 μm green PSL. **D** Optical microscopy image (40×) of the light green region of the sediment in **B** after dilution with DI water. The image shows a mixture of 3 and 4 μm particles.

Top Layer Composition: 100% 3 μm green PSL.

Bottom Layer Composition: 63.1% ± 2.7% 4 μm white PSL

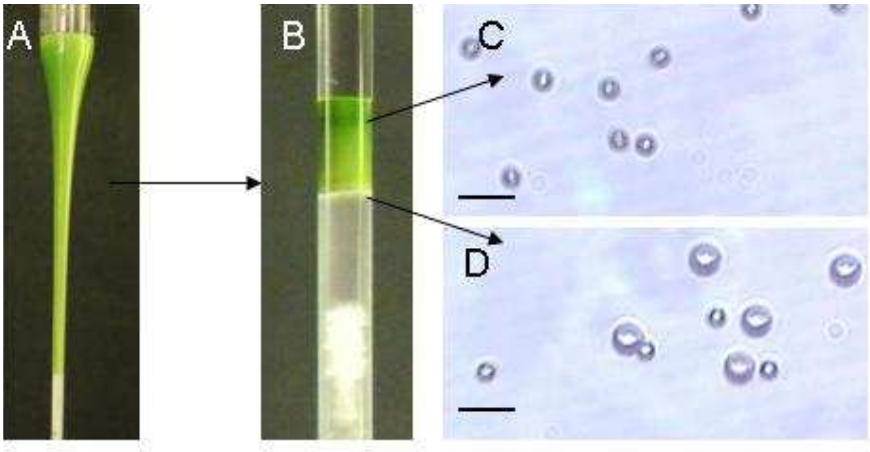

Figure A.6. Particle recovery of the sediment produced by sedimentation at 1g of a mixture of 3 and 4.9 μm polystyrene particles. All the scale bars at the bottom left of the images are 10 μm. **A** Mixture of 1:1 volume ratio of 3 μm green and 4.9 μm white sulfate-functionalized PSL particles at 0.01 volume fraction. **B** Resulting sediment of the mixture in **A** after sedimentation in gravity (1g) for 5 days. The white region at the bottom is wax sealing the glass capillary. **C** Optical microscopy image (40×) of the dark green region of the sediment in **B** after dilution with DI water. All the particles are 3 μm green PSL. **D** Optical microscopy image (40×) of the light green region of the sediment in **B** after dilution with DI water. The image shows a mixture of 3 and 4.9 μm particles.

Top Layer Composition: 100% 3 μm green PSL.

Bottom Layer Composition: 67.9% ± 2.6% 4.9 μm white PSL

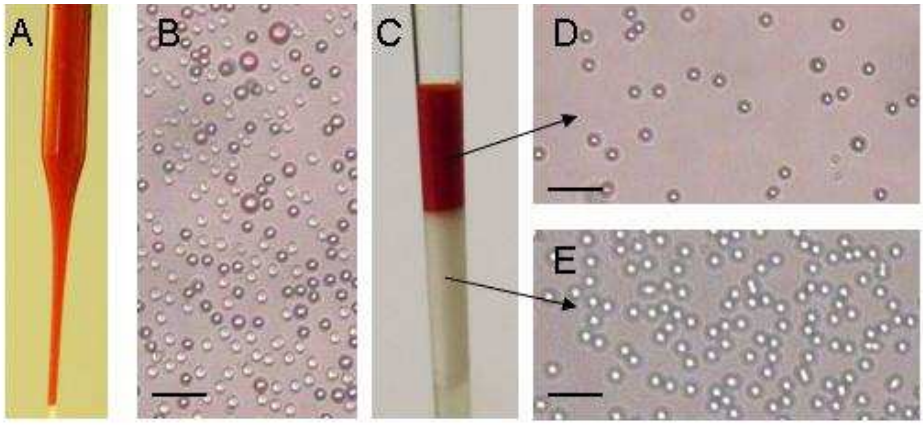

Figure A.7 Particle recovery of the sediment produced by sedimentation at 1g of a mixture of 3 μm silica and 3 μm polystyrene particles. All the scale bars at the bottom left of the images are 10 μm. **A** Mixture of 1:1 volume ratio of 3 μm white silica and 3 μm red sulfate-functionalized PSL particles at 0.01 volume fraction. **B** Optical microscopy image (40×) of the mixture in **A** after dilution to 10^{-4} volume fraction. **C** Resulting sediment of the mixture in **A** after sedimentation in gravity (1g) for 3 days. The white region at the bottom is wax sealing the glass capillary. **D** Optical microscopy image (40×) of the red region of the sediment in **C** after dilution with DI water. All the particles are 3 μm red PSL. **E** Optical microscopy image (40×) of the white region of the sediment in **C** after dilution with DI water. All the particles are 3 μm white silica.

Top Layer Composition: 100% 3 μm red PSL.

Bottom Layer Composition: 100% 3 μm white silica

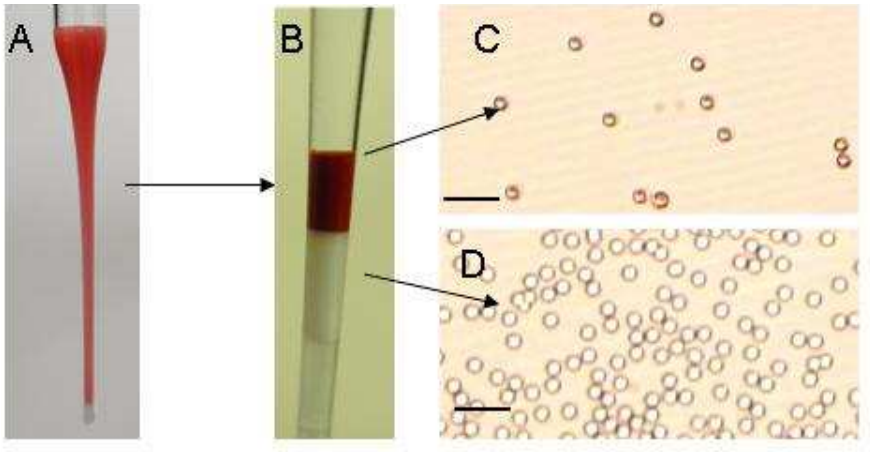

Figure A.8. Particle recovery of the sediment produced by sedimentation at 1000g of a mixture of 3 μm silica and 3 μm polystyrene particles. All the scale bars at the bottom left of the images are 10 μm. **A** Mixture of 1:1 volume ratio of 3 μm white silica and 3 μm red sulfate-functionalized PSL particles at 0.01 volume fraction. **B** Resulting sediment of the mixture in **A** after centrifugation at 1000g for 30 minutes. The white region at the bottom is wax sealing the glass capillary. **C** Optical microscopy image (40×) of the red region of the sediment in **B** after dilution with DI water. All the particles are 3 μm red PSL. **D** Optical microscopy image (40×) of the white region of the sediment in **B** after dilution with DI water. All the particles are 3 μm white silica.

Top Layer Composition: 100% 3 μm red PSL.

Bottom Layer Composition: 100% 3 μm white silica

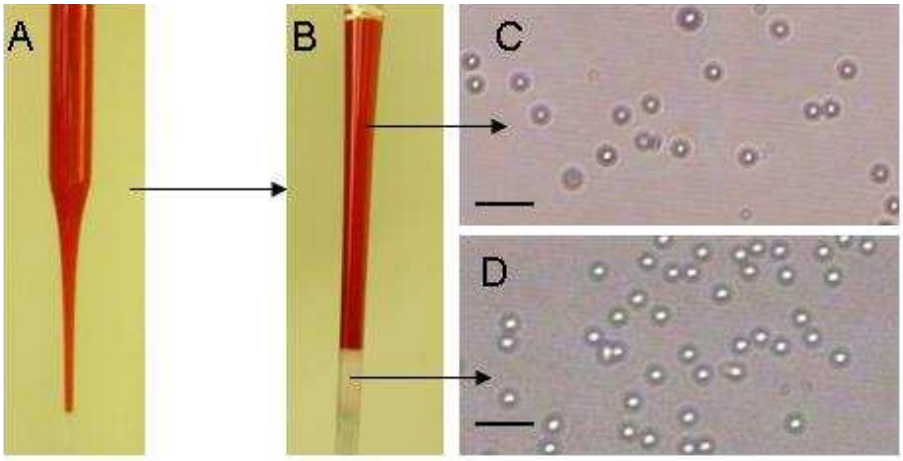

Figure A.9. Particle recovery of the sediment produced by sedimentation at 1g of a mixture of 3 μm silica and 3 μm polystyrene particles (1:9 volume ratio). All the scale bars at the bottom left of the images are 10 μm. **A** Mixture of 1:9 volume ratio of 3 μm white silica and 3 μm red sulfate-functionalized PSL particles at 0.01 volume fraction. **B** Resulting sediment of the mixture in **A** after sedimentation in gravity (1g) for 5 days. The white region at the bottom is wax sealing the glass capillary. **C** Optical microscopy image (40×) of the red region of the sediment in **B** after dilution with DI water. All the particles are 3 μm red PSL. **D** Optical microscopy image (40×) of the white region of the sediment in **B** after dilution with DI water. All the particles are 3 μm white silica.

Top Layer Composition: 100% 3 μm red PSL.

Bottom Layer Composition: 100% 3 μm white silica

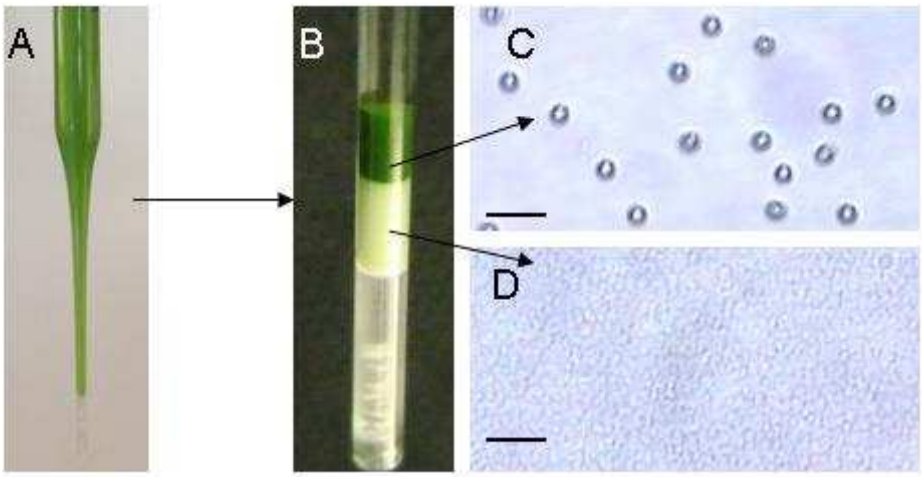

Figure A.10. Particle recovery of the sediment produced by sedimentation at 1g of a mixture of 3 μm silica and 0.9 μm polystyrene particles. All the scale bars at the bottom left of the images are 10 μm. **A** Mixture of 1:1 volume ratio of 0.9 μm white silica and 3 μm green sulfate-functionalized PSL particles at 0.01 volume fraction. **B** Resulting sediment of the mixture in **A** after sedimentation in gravity (1g) for 5 days. The white region at the bottom is wax sealing the glass capillary. **C** Optical microscopy image (40×) of the green region of the sediment in **B** after dilution with DI water. All the particles are 3 μm green PSL. **D** Optical microscopy image (40×) of the white region of the sediment in **B** after dilution with DI water. The particle concentration of this image is high. All the particles are 0.9 μm white silica.

Top Layer Composition: 100% 3 μm red PSL.

Bottom Layer Composition: 100% 0.9 μm white silica

Appendix B

Model of the Minimum Potential Energy

```
(* Import Packing Fraction data on radius ratio and volume ratio*)
phi = ListInterpolation[{{0.64, 0.64, 0.64, 0.64,
     0.64, 0.64, 0.64, 0.64, 0.64, 0.64, 0.64},
    {0.64, 0.665, 0.675, 0.678, 0.677, 0.675,
     0.668, 0.663, 0.658, 0.65, 0.64},
    {0.64, 0.685, 0.708, 0.712, 0.71, 0.702,
     0.69, 0.68, 0.667, 0.655, 0.64},
    {0.64, 0.7, 0.74, 0.745, 0.735, 0.72,
     0.705, 0.69, 0.675, 0.657, 0.64},
    {0.64, 0.71, 0.757, 0.767, 0.753, 0.738,
     0.72, 0.698, 0.677, 0.66, 0.64}}, {{1, 5}, {0, 1}}];
Plot3D[phi[rr, fs], {rr, 1, 5}, {fs, 0, 1}]
```

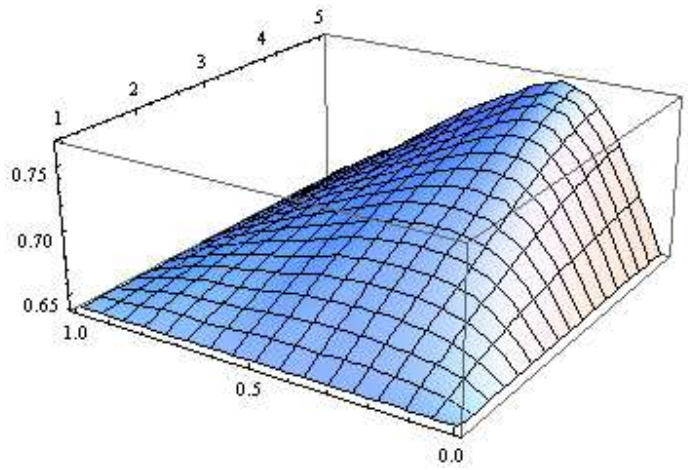

```
(* Set Initial conditions *)
(* Particle conditions *)

as = 1.5×10^-6; (*small particle size, m*)
al = 2×10^-6; (*large particle size, m*)
ρsp = 1055; (*small particle density, kg/m3*)
ρlp = 1055; (*large particle density, kg/m3*)
fs0 = 0.5; (*initial particle volume ratio*)
phi0 = 0.01; (*initial volume fraction*)



(*Solution conditions*)
ρf = 998.23; (*fluid density, kg/m3*)
ki = 80×10^-9; (*debye length in packed particle fluid, m*)
g = 9.8; (*gravitational/centrifugal acceleration, m/s*)
T = 293; (*temperature, K*)
k = 1.38065×10^-23 ; (*Boltzmann constant, J/K*)


(*Vessel dimensions*)
As = 7.854×10^-7; (*cross sectional area, m2*)
h0 = 200×10^-2; (*initial height, m*)

(*calculate knowns*)
ms = As*h0*phi0*fs0*ρsp; (*total mass of small particles, kg*)
ml = As*h0*phi0*(1-fs0)*ρsp; (*total mass of large particles, kg*)
mw = As*h0*(1-phi0)*ρf; (* total fluid mass, kg*)
ρs = (as/(as+ki))^3*(ρsp-ρf)+ρf; (*effective density small, kg/m3*)
ρl = (al/(al+ki))^3*(ρlp-ρf)+ρf; (*effective density large, kg/m3*)
rr = ((al+ki)/(as+ki)); (*radius ratio*)

(*define heights in terms of fs1 & fs2 - from the mass balance*)
h1 = Function[{fs1, fs2}, h0*phi0/phi[rr, fs1]*(fs0-fs2)/(fs1-fs2)];
h2 = Function[{fs1, fs2}, h0*phi0/phi[rr, fs2]*(fs0-fs1)/(fs2-fs1)];
h3 = Function[{fs1, fs2}, h0*(1-phi0)-h1[fs1, fs2]*(1-phi[rr, fs1])
    -h2[fs1, fs2]*(1-phi[rr, fs2])];
```

```
(*potential energy calculation*)
delE = Function[{fs1, fs2}, As * g / 2 *
    (phi[rr, fs1] * (ρl - ρf + (fs1) (ρs - ρl)) * h1[fs1, fs2]^2 +
      phi[rr, fs2] * (ρl - ρf + (fs2) (ρs - ρl)) *
       ((h2[fs1, fs2] + h1[fs1, fs2])^2 - h1[fs1, fs2]^2))];

(*entropic contribution to free energy*)
delS = Function[{fs1, fs2}, k * T * As * 3 / (4 π) *
    (h1[fs1, fs2] * phi[rr, fs1] *
       (fs1 / as^3 * Log[fs1 / (fs1 + (1 - fs1) as^3 / al^3)] +
         (1 - fs1) / al^3 * Log[1 - fs1 / (fs1 + (1 - fs1) as^3 / al^3)]) +
      h2[fs1, fs2] * phi[rr, fs2] *
       (fs2 / as^3 * Log[fs2 / (fs2 + (1 - fs2) as^3 / al^3)] +
         (1 - fs2) / al^3 * Log[1 - fs2 / (fs2 + (1 - fs2) as^3 / al^3)]))];

(*interparticle forces contribution to free energy*)
delP = (As * h0 * phi0 * fs0 / (4 / 3 * Pi * as^3) + As * h0 * phi0 * (1 - fs0) / (4 / 3 * Pi * al^3)) * 6 * 2;
```

```
(*Minimization of the total energy*)
min = Minimize[{delE[fs1, fs2] + delS[fs1, fs2] + delP, h1[fs1, fs2] ≥ 0,
    h2[fs1, fs2] ≥ 0, fs1 ≥ 0, fs2 ≥ 0, fs1 ≤ 1, fs2 ≤ 1, fs1 ≠ fs2}, {fs1, fs2}];
delEf = delE[fs1, fs2] * 1 / (k × T) /. min[[2]];
delGf = delS[fs1, fs2] * 1 / (k × T) /. min[[2]];
h1f = h1[fs1, fs2] /. min[[2]];
h2f = h2[fs1, fs2] /. min[[2]];
h3f = h3[fs1, fs2] /. min[[2]];
Graphics[{RGBColor[1 - fs1, fs1, 0] /. min[[2]], Rectangle[{0, 0},
   {(h1f + h2f) / 5, h1f}], RGBColor[1 - fs2, fs2, 0] /. min[[2]],
  Rectangle[{0, h1f}, {(h1f + h2f) / 5, h1f + h2f}]}]

Print["The height of the supernatant section is ", h3f * 1000, " mm."]
Print["The height of the upper section is ", h2f * 1000, " mm."]
Print["The composition of the upper section is ", fs2 * 100 /. min[[2]],
 "% small particles"]
Print["The height of the lower section is ", h1f * 1000, " mm."]
Print["The composition of the lower section is ", fs1 * 100 /. min[[2]],
 "% small particles"]
Print["The relative gravitational potential energy is ", delEf, " kT."]
Print["The relative entropic potential energy is ", delGf, " kT."]
Print["The relative interparticle interaction energy is ", delP, " kT."]
Print["The final minimum free energy is ", delGf + delEf + delP, " kT."]
```

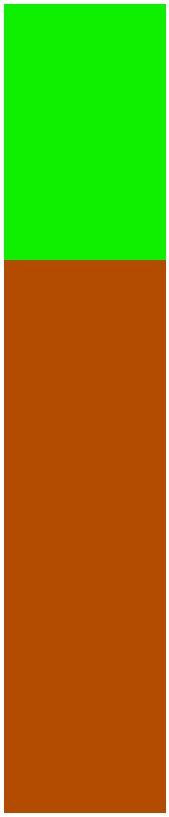

The height of the supernatant section is 1969.2 mm.
The height of the upper section is 9.73512 mm.
The composition of the upper section is 93.8657% small particles
The height of the lower section is 21.0641 mm.
The composition of the lower section is 30.0482% small particles
The relative gravitational potential energy is 2.87684×10^{13} kT.
The relative entropic potential energy is -3.56672×10^{8} kT.
The relative interparticle interaction energy is 9.47919×10^{9} kT.
The final minimum free energy is 2.87775×10^{13} kT.

Appendix C

Measurement of the Singlet-Doublet Packing Fraction

C.1 Introduction

In this document we have previously shown that the packing fraction of the particles to sort plays a key role in the separation process. In order to apply this knowledge to sorting of colloidal mixtures of singlets and doublets it is critical to know how they pack both individually and together. Zou et al[1] reported in 2009 that the packing fraction of doublets is lower than the packing fraction of single spheres. However, no packing fraction data is available for mixtures of singlets and doublets. In order to study such behavior Kristi Ann Wegener and Tawana Hines measured the macroscopic packing fraction of millimeter size singlets and doublets.

C.2 Materials and Methods

C.2.1 Materials

Ultrasonic BBs 10,000 rds Translucent Green were bought from Softair® USA (Dallas, TX) to analyze the singlets - doublets packing fraction (see Figure C.1). A 2.9 L Sterilite plastic graduated cylinder was used to pack the particles and a VM-3000 mini vortexer bought from VWR International was used to shake the container. The Original Super Glue was used to produce the doublets.

Figure C.1 Material used for the measurement of the singlets-doublets packing fraction. The green BB's are on the right of the image. The container used for the measurement with some BB's is on the left.

To measure the BB's diameter a palmer Mitutoyo Stainless Hardened MN.85 was used. To measure the BB's mass a balance Mettler Toledo AB204 was used.

C.2.2 Fabrication of doublets

The macroscopic doublets were made by easily attaching two BBs together using The Original Super Glue gel. The BB's were placed in V-shaped piece of paper to have a better alignment of the particles. The glued BB's were cured for 24 hours before being used in the packing fraction experiments.

C.2.3 Measurement of the packing fraction

Using the graduated cylinder 1500 ml of water was measured. This water was poured into the plastic container and a 1.5 l volume reference line was drawn for the measurement of BBs. In order to measure the particle packing the following procedure was followed. First, the Sterilite plastic container was weighed using the balance. Then it

was filled with the desired mixture of BB's until the 1.5 l line was reached. Then the container was placed on the vortexer for 30 seconds to allow reorganization of the particles (see Figure C.2). The mixture was leveled again to the 1.5 L line previously marked and placed for another 30 seconds on the vortexer. Next the container was weighted again to determine the total weight of BBs in the sample. This procedure is repeated 10 times for each mixture proportion.

Figure C.2 Measurement of the singlets-doublets packing fraction. The plastic container filled with BB's until the line of 1.5 L was placed on the vortexer to pack the particles tightly.

C.3 Characterization of the singlets and doublets

The average diameter of the singles and the long axis of the doublets were measured using the palmer. Tables C.1 and C.2 show the measurements for single and doublet BB's respectively.

Table C.1 Measurements of the singlet BB diameter.

Singlet BB diameter (mm)				
5.9	5.9	5.8	5.9	5.9
5.9	5.9	5.9	5.9	5.9
5.9	5.9	5.9	5.9	5.95
5.9	5.9	5.9	5.9	5.9
5.85	5.9	5.9	5.9	5.9
Average	**5.896**	Standard Deviation		0.025

Table C.2 Measurements of the doublet BB long axis.

Doublet BB long axis (mm)				
11.74	11.825	11.76	11.86	11.79
11.825	11.79	11.85	11.8	11.84
Average	**11.808**	Standard Deviation		0.04

Also measurements of mass of singlets and doublets were performed. Mass measurements of 5 singlets BB's are shown in Table C.3. Measurements of a doublet BB's mass is shown in table C.4.

Table C.3 Measurements of mass of groups of 5 singlet BB.

Singlet BB mass (g)				
0.5518	0.5503	0.559	0.5515	0.5555
0.5514	0.5453	0.5469	0.552	0.5493
0.548	0.5535	0.5514	0.5534	0.5557
0.5498	0.5503	0.5578	0.5513	0.554
0.5525	0.5545	0.5541	0.5554	0.5557
Average	**0.5524**	Standard Deviation		0.0033

Table C.4 Measurements of mass of doublet BB's.

Doublet BB mass (g)				
0.2242	0.2264	0.2238	0.228	0.2286
0.2249	0.2225	0.2247	0.2264	0.2203
0.223	0.2223	0.2267	0.2234	0.2265
0.2273	0.2233	0.2231	0.2248	0.2242
0.222	0.2216	0.2317	0.2271	0.228
Average	**0.225**	Standard Deviation		0.0026

From the data of Tables C.1, C.2, C.3 and C.4 we can conclude that the glue used to create the doublets is adding increasing the mass and the length of the doublets respect to two singlets together.

C.4 Results

Before showing the experimental results of the measurement of packing fraction, let us explain the data treatment procedure. First the mass of the empty plastic container and the mass of the plastic container plus BB's were measured (see Section C.2.3). The mass of the container is subtracted from the mass of the container plus BB's to know the total mass of BB´s. Then, the value of the total mass of BBs m_{tot} is divided by the average mass of a single BB in the sample m_{avg}, obtaining the number of spheres in the container

$n_{BB's}$ The value of m_{avg} is calculated considering the proportion of singlets in the sample R_S, the mass of a doublet m_D and the mass of a singlet m_S.

$$\frac{m_{tot}}{m_{avg}} = n_{BB's} \tag{C.1}$$

$$m_{avg} = m_S R_S + \frac{m_D}{2}(1 - Rs) \tag{C.2}$$

The total volume occupied by solids $V_{BB's}$ is calculated by knowing the number of spheres in the container and their average diameter d_{avg}. The value of d_{avg} is calculated considering the proportion of singlets in the sample R_S, the long axis of a doublet d_D and the diamter of a singlet d_S. Finally, the packing fraction of the sample ϕ is obtained by dividing the total volume occupied by solids by the total volume V_T (1.5 l).

$$V_{BB's} = n_{BB's} \times \frac{4}{3}\pi\left(\frac{d_{avg}}{2}\right)^3 \tag{C.3}$$

$$d_{avg} = d_S R_S + \frac{d_D}{2}(1 - Rs) \tag{C.4}$$

$$\phi = \frac{V_{BB's}}{V_T} \tag{C.5}$$

These equations and the experimental data allow us to calculate the packing fraction of any desired mixture of singlets and doublets. First the technique was validated by measuring the packing fraction of singlets and comparing that value with the literature (see Table C.5).

Table C.5 Experimental data for the packing fraction of 100% singlets.

Run #	1	2	3	4	5	6	7	8	9	10
Container mass	177.9	177.9	178.0	177.9	178.0	177.9	178.0	177.9	177.9	177.9
Total mass	1176	1168	1171	1147	1177	1165	1152	1145	1175	1161
Packing fraction	0.646	0.641	0.644	0.627	0.647	0.639	0.630	0.626	0.645	0.637
Average Packing fraction			**0.638**	Standard Deviation						0.008

The average packing fraction found is 0.638 ± 0 006. A comparison with the data for monodisperse spheres from Table 2.1 shows that the known value is 0.64. We can conclude that this technique is reliable to measure the packing fraction of granulate systems.

Once the technique was validated, 10 mixtures with different proportions of singlets and doublets were analyzed: 10%, 20%, 30%, 40%, 50%, 60%, 70%, 80%, 90% and 100% of doublets (number fraction). See Tables C.6 to C.15 for data.

Table C.6 Experimental data for the packing fraction of 100% doublets.

Run #	1	2	3	4	5	6	7	8	9	10
Container mass	178.0	178.2	178.1	178.1	178.1	178.1	178.2	178.2	178.3	178.2
Total mass	1068	1093	1081	1090	1078	1077	1081	1076	1080	1084
Packing fraction	0.566	0.582	0.574	0.580	0.572	0.572	0.574	0.571	0.573	0.576
Average Packing fraction			**0.574**	Standard Deviation						0.005

Table C.7 Experimental data for the packing fraction of 90% doublets.

Run #	1	2	3	4	5	6	7	8	9	10
Container mass	178.0	178.1	178.0	178.1	178.1	178.0	178.1	178.1	178.0	178.1
Total mass	1081	1115	1101	1116	1094	1107	1098	1086	1092	1098
Packing fraction	0.575	0.597	0.588	0.597	0.584	0.592	0.586	0.579	0.582	0.586
Average Packing fraction			**0.587**	Standard Deviation						0.007

Table C.8 Experimental data for the packing fraction of 80% doublets.

Run #	1	2	3	4	5	6	7	8	9	10
Container mass	178.1	178.0	178.0	178.1	178.0	178.1	178.1	178.0	178.0	178.0
Total mass	1095	1109	1093	1105	1102	1100	1097	1111	1116	1101
Packing fraction	0.585	0.594	0.584	0.592	0.590	0.589	0.587	0.596	0.599	0.589
Average Packing fraction			**0.590**	Standard Deviation						0.005

Table C.9 Experimental data for the packing fraction of 70% doublets.

Run #	1	2	3	4	5	6	7	8	9	10
Container mass	177.9	178.0	178.1	178.1	178.1	178.1	178.0	178.0	178.1	178.0
Total mass	1105	1128	1112	1106	1121	1119	1128	1114	1109	1122
Packing fraction	0.592	0.608	0.597	0.593	0.603	0.601	0.608	0.598	0.595	0.604
Average Packing fraction			**0.600**	Standard Deviation						0.006

Table C.10 Experimental data for the packing fraction of 60% doublets.

Run #	1	2	3	4	5	6	7	8	9	10
Container mass	177.9	177.9	177.9	177.9	177.9	177.9	177.9	177.9	177.9	177.9
Total mass	1107	1116	1107	1107	1118	1120	1113	1124	1133	1103
Packing fraction	0.595	0.601	0.595	0.595	0.602	0.603	0.599	0.606	0.612	0.592
Average Packing fraction			**0.600**	Standard Deviation						0.006

Table C.11 Experimental data for the packing fraction of 50% doublets.

Run #	1	2	3	4	5	6	7	8	9	10
Container mass	177.9	177.9	177.9	177.9	177.9	177.9	177.9	177.9	177.9	177.9
Total mass	1123	1131	1122	1126	1131	1116	1124	1120	1119	1137
Packing fraction	0.607	0.612	0.606	0.609	0.612	0.602	0.607	0.605	0.604	0.616
Average Packing fraction			**0.608**				Standard Deviation			0.004

Table C.12 Experimental data for the packing fraction of 40% doublets.

Run #	1	2	3	4	5	6	7	8	9	10
Container mass	177.9	177.9	177.9	177.9	177.9	177.9	177.9	177.9	177.9	177.9
Total mass	1127	1138	1116	1138	1100	1118	1121	1134	1122	1128
Packing fraction	0.619	0.628	0.626	0.607	0.620	0.622	0.612	0.613	0.603	0.623
Average Packing fraction			**0.613**				Standard Deviation			0.008

Table C.13 Experimental data for the packing fraction of 30% doublets.

Run #	1	2	3	4	5	6	7	8	9	10
Container mass	177.9	177.9	177.9	177.9	177.9	177.9	177.9	177.9	177.9	177.9
Total mass	1160	1136	1150	1130	1128	1144	1152	1138	1138	1141
Packing fraction	0.616	0.625	0.630	0.635	0.618	0.640	0.631	0.623	0.622	0.627
Average Packing fraction			**0.624**				Standard Deviation			0.007

Table C.14 Experimental data for the packing fraction of 20% doublets.

Run #	1	2	3	4	5	6	7	8	9	10
Container mass	180.1	177.9	177.9	177.9	177.9	177.9	177.9	177.9	177.9	177.9
Total mass	1152	1163	1151	1143	1153	1153	1142	1154	1140	1148
Packing fraction	0.627	0.636	0.628	0.623	0.629	0.629	0.622	0.630	0.621	0.626
Average Packing fraction			**0.627**				Standard Deviation			0.004

Table C.15 Experimental data for the packing fraction of 10% doublets.

Run #	1	2	3	4	5	6	7	8	9	10
Container mass	177.9	177.9	177.9	177.9	177.9	177.9	177.9	177.9	177.9	177.9
Total mass	1173	1165	1171	1159	1132	1150	1151	1156	1151	1153
Packing fraction	0.643	0.638	0.642	0.634	0.617	0.628	0.629	0.632	0.629	0.630
Average Packing fraction			**0.632**	Standard Deviation						0.008

All the date from these tables has been collected in Figure C.3 to show the variation of the packing fraction with the percentage of doublets.

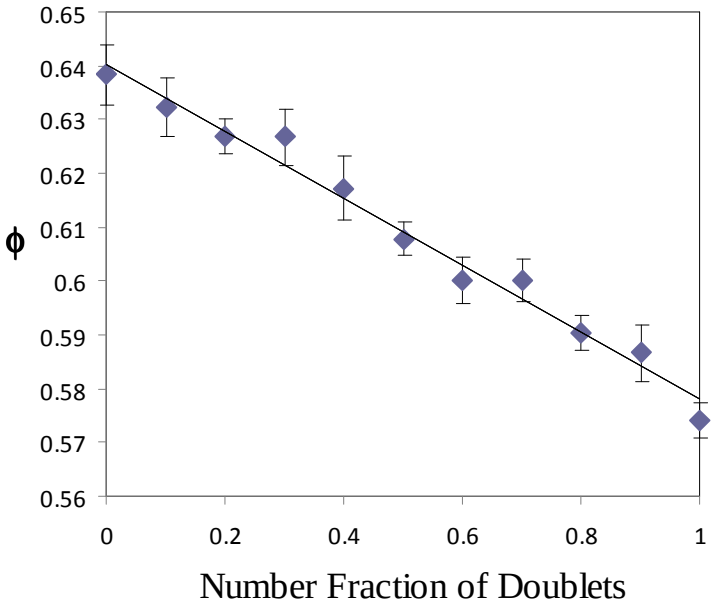

Figure C.3 Packing fraction of mixtures of singlets and doublets. Data collected from tables C.6 to C.15.

It is important to address that during the shaking procedure to study the packing fraction some doublets broke apart. Once all the packing fraction measurements were

done, we discovered that 22% of the total number of doublets were broken. This could affect the measurements of the packing fraction.

C.5 Discussion

Figure C.3 shows that packing fraction of a mixture of singlets and doublets changes linearly with the number of doublets in the sample. Another important implication is that the packing fraction of pure doublets of any mixture containing doublets is lower than the packing fraction of singlets. This result has important implications in the sorting procedure studied in this thesis. The difference in packing fraction between sinlgets and doublets can be used as a leading force for separation.

C.6 References

[1] Zou, L. N., Cheng, X., Rivers, M.L., Jaeger, H. M., Nagel, S.R. *Science* **326**, 408-410 (2009).